

10-29-2010

Finite Element Analysis of Thermoelectric Systems with Applications in Self Assembly and Haptics

Patrick T. McKnight
University of South Florida

Follow this and additional works at: <http://scholarcommons.usf.edu/etd>

 Part of the [American Studies Commons](#)

Scholar Commons Citation

McKnight, Patrick T., "Finite Element Analysis of Thermoelectric Systems with Applications in Self Assembly and Haptics" (2010).
Graduate Theses and Dissertations.
<http://scholarcommons.usf.edu/etd/3630>

This Thesis is brought to you for free and open access by the Graduate School at Scholar Commons. It has been accepted for inclusion in Graduate Theses and Dissertations by an authorized administrator of Scholar Commons. For more information, please contact scholarcommons@usf.edu.

Finite Element Analysis of Thermoelectric Systems
with Applications in Self Assembly and Haptics

by

Patrick T. McKnight

A thesis submitted in partial fulfillment
of the requirements for the degree of
Master of Science in Mechanical Engineering
College of Engineering
University of South Florida

Major Professor: Nathan Crane, Ph.D.
Frank Pyrtle, Ph.D.
Kyle Reed, Ph.D.

Date of Approval:
October 29, 2010

Keywords: ansys, three-dimensional FEA, peltier effect, energy conversion, thermal grill
illusion

© Copyright 2010, Patrick T. McKnight

Acknowledgements

Utmost gratitude goes to my major professor, Dr. Nathan Crane for supporting my academic career and going beyond the call of duty to support my time at USF. Dr. Crane is a true and gifted educator, and I am fortunate to have been given the opportunity to work under him.

Dr. Kyle Reed deserves many thanks, for his patience and always being available for help while designing the haptic display.

I am also grateful for having parents who have supported my life as well as academics for as long as I can remember. Without an analytical, engineering mind-state being instilled from an early age, this may not have been possible.

I would finally like to thank my friends in the mechanical engineering department, Ardit Agastra and Caroline Liberti for always being available for discussion about topics we sometimes knew little about. A willingness to learn, no matter what the subject, was not only beneficial, but also entertaining. Also appreciated are my lab mates, Jose Caraballo, Gary Hendrick, Corey Lynch and James Tuckerman for keeping things interesting during the long hours spent in the Kopp basement.

Table of Contents

List of Tables	ii
List of Figures	iii
ABSTRACT	v
Chapter 1 - Introduction.....	1
1.1 Thesis Statement	1
1.2 Background	1
1.2.1 The Thermoelectric Effect	1
1.2.2 Self-assembly	4
1.2.3 Thermal Haptics and the Thermal Grill Effect	5
1.3 Literature Review – Theory of the Thermoelectric Effect.....	8
1.3.1 Materials	12
1.4 Thesis Outline	13
Chapter 2 – Three-dimensional FEA Analysis	14
2.1 Three-dimensional Thermoelectric Modeling in Ansys v12.1	14
2.2 Verification of the Ansys Model against Generalized Thermoelectric System Theory	20
Chapter 3 - Analysis of Three-dimensional Self-assembled Devices.....	26
3.1 Description of the Three-dimensional Finite Element System	26
3.2 Self-assembled Configurations of Missing, Centrally Located Elements	30
3.3 Review of Results from Three-dimensional Ansys Analyses.....	31
3.4 Discussion of Results	33
Chapter 4 – Haptic Thermal Display	37
4.1 Design Requirements	37
4.2 Design and Components Used	38
4.3 Simulated Performance	42
4.4 Next Steps in Device Development	47
Chapter 5 – Conclusions and Recommendations for Advancement.....	49
List of References	52
Appendices.....	55
Appendix A – Ansys Batch Code	56
Appendix B – Matlab Analytical Solutions Code.....	67

List of Tables

Table 1 – Characteristic dimensions for a 6x6 array with a fill factor of 0.9	17
Table 2 – System properties for Bi ₂ Te ₃ based analysis	19
Table 3 – Key system properties and parameters used in the analysis of a three dimensional thermoelectric device	28
Table 4 – Results extracted from the Ansys solution for traditional performance analysis.....	33
Table 5 – Performance and efficiency comparison between closely packed elements verses less closely packed elements under equal boundary conditions.....	35

List of Figures

Figure 1 – Simple thermocouple design	8
Figure 2 – A closed thermoelectric circuit.....	9
Figure 3 – Basic thermoelectric circuit.....	10
Figure 4 – Diagram of occupied electron states in a semiconductor with impurities.	13
Figure 5 – Design schematic of 6x6 array with a redundancy of 4.	17
Figure 6 – 3D Mesh of a 6x6 thermoelectric cooler with a redundancy of 4.	18
Figure 7 – Simple generalized thermoelectric system.	21
Figure 8 – Methodology for equating entry substrate conductance to an equivalent conductivity that includes thermal contact resistance.....	22
Figure 9 – Plot of analytical and FEA solutions of thermoelectric performance with constant boundaries temperatures T_S and T_A and varied current input.	22
Figure 10 – Temperature plots for varying boundary temperatures where (a) T_S is held constant and T_A varies from 315 K to 375 K, and (b) T_A is held constant and T_S varies from 250 K to 310 K.	24
Figure 11 – Comparison of heat flux at the cold-side junction under conditions of varying T_A and T_S	25
Figure 12 – Assigned thermoelectric volume numbers and locations for a 6x6 array and redundancy of 4.....	27
Figure 13 – Description of the paths for temperature profile plots	29
Figure 14 – Temperature profiles plotted along (a) Path A and Path B, and (b) Path C at the hot and cold sides.	29

Figure 15 – (a) Control case with full assembly (b) Case 1 with one center element missing, (c) Case 2 with two center elements missing, (d) Case 3 with three center elements missing.	31
Figure 16 – Path A and Path B temperature profiles for (a) the fully assembled control case, (b) one central missing element, (c) two central missing elements, and (d) three central missing elements.	32
Figure 17 – Path C temperature profiles along the hot-side junction surface (a) for a fully assembled case, (b) with one central element missing, (c) two central elements missing, and (d) three central elements missing.	32
Figure 18 – Path C temperature profiles along the cold-side junction surface (a) for a fully assembled case, (b) with one central element missing, (c) two central elements missing, and (d) three central elements missing.	33
Figure 19 – (a) Schematic of thermoelectric array with discretely controlled element rows, (b) Top view of the display, (c) Side-view of the thermal display.....	39
Figure 20 – Design section for a proposed thermal display.	40
Figure 21 – Control flowchart for a thermal display with five independent thermoelectric rows.....	41
Figure 22 – Transient temperature control of five independent rows of thermoelectric elements.	42
Figure 23 – Comparison of temperature profiles in the direction of heat flow for a coarse mesh and fine mesh size.	44
Figure 24 – Components and design of the FEA model simulating a haptic device on skin tissue.	44
Figure 25 – (a) Temperature profile at the epidermis-dermis interface when the third thermoelectric row is at a maximum value, (b) Plot of the profile at the center of an element in Row 3.....	45
Figure 26 – Description of the orientation of discretely controlled thermoelectric rows.....	46
Figure 27 – (a) Plot of temperature profile along the interface between the epidermis and dermis.	47

ABSTRACT

Micro-scale self assembly is an attractive method for manufacturing sub-millimeter sized thermoelectric device parts. Challenges controlling assembly yield rates, however, have caused research to find novel ways to implement the process while still resulting in a working device. While a typical system uses single n-type and p-type material elements in series, one method used to increase the probability of a working device involves adding redundant parallel elements in clusters. The drawback to this technique is that thermal performance is affected in clusters which have missing elements. While one-dimensional modeling sufficiently describes overall performance in terms of average junction temperatures and net heat flux, it fails when a detailed thermal profile is needed for a non-homogeneous system. For this reason, a three-dimensional model was created to describe thermal performance using Ansys v12.1. From the results, local and net performance can be described to help in designing an acceptable self-assembled device.

In addition, a haptic thermal display was designed using thermoelectric elements with the intention of testing the thermal grill illusion. The display consists of 5 electrically independent rows of thermoelectric elements which are controlled using pulse width modulating direct current motor controllers.

Chapter 1 - Introduction

1.1 Thesis Statement

This thesis is presented to show the use of finite element analysis (FEA) for the thermoelectric performance of micro-scale, self-assembled devices. Previous research has demonstrated an optimal performance at scales inaccessible to pick and place manufacturing and thin film deposition methods. While self-assembly shows promise, 100% assembly of components is not expected and thus, the final configuration of a device could take on many forms. This paper hopes to capture the subsequent performance characteristics due to the non-homogeneities.

An additional project was undertaken to design a haptic thermal display using macro thermoelectric elements which are controlled by a DC motor controller with a pulse width modulated (PWM) voltage output. Analysis of the design was done using FEA to study the expected thermal gradient the test subject would observe. Various other details related to the design are also described as well.

1.2 Background

1.2.1 The Thermoelectric Effect

In 1821, the thermoelectric effect was discovered by German physicist Thomas Seebeck. He noticed an electromotive force, causing a small voltage potential, when a junction of two dissimilar metals was heated. More importantly, it was realized that the

change in potential was a function of the change in temperature [1], and unlike pyroelectrics, the voltage produced is maintained as long as a temperature difference exists. About a decade later, a French watchmaker, Jean Carlos Peltier discovered that if the experiment is run in reverse, a small change in temperature could be produced when a current was applied to the junction. He also noticed that when the current direction was inverted, the heating and cooling of the dissimilar metals was reversed. It should be noted that because purely metallic materials were all that were available at the time, this effect was very small, and Joule heating easily disguised the thermoelectric effects.

Furthermore, William Thomson contributed to the development by realizing the two effects found by Seebeck and Peltier were related to one another. By applying thermodynamic principles to the two situations, Thomson found that the two dissimilar materials were not a requirement to observe thermoelectricity, and that in a third case, a homogeneous conductor could be heated and cooled with the application of a current source, or develop a voltage potential with the application of a temperature gradient [2].

These discoveries paved the way for inventions like the thermocouple, thermoelectric power generator (TEG), and thermoelectric refrigerator/cooler (TEC).

Thomson's success in quantifying the effect yielded a set of equations, which will be outlined later in the text, which related the three thermoelectric effects. Coefficients were defined for Seebeck, Peltier and Thomson. The important thing to realize about the three coefficients is that the Seebeck and Peltier refer to a junction between two different materials, whereas the Thomson coefficient refers to a single, bulk conductor.

Considering thermoelectricity is one of multiple thermodynamic effects occurring simultaneously when current is passed through a material, a method had to be devised to

measure the properties without effects like Joule heating present. The answer was to use a superconductor as one of the two materials. Since superconductors possess zero electrical resistance, they theoretically also have a Seebeck and Peltier coefficient of zero. Where before a differential coefficient had to be defined between two materials, now absolute coefficients could be used based on the zero-reference. This is justified by applying the third law of thermodynamics, which shows that the differential Seebeck coefficient between two conductors must be zero at 0 °K. Furthermore, Borelius et al. [3] experimentally determined the absolute Seebeck coefficient of lead from 0 °K up to 18 °K, then determined the Thomson coefficient from 18 °K to room temperature. By doing this, the absolute Seebeck coefficient of lead was found over the entire range of temperatures, thus allowing future experiments to use lead as a reference material, and negating the need of a superconductor in the experiment.

In the early 1900's, metals were still considered to exhibit the best thermoelectric properties. It had been shown mathematically that a good thermoelectric material should have a high Seebeck coefficient, high electrical conductivity, and low thermal conductivity [4]. These characteristics minimize the thermal effects of Joule heating and dampen the effects of the parasitic heat path which is opposite the direction of heat pumping. In quantitative terms, it was shown that practical refrigeration and power generation would be possible with materials, which hadn't been invented yet, possessing optimal properties.

With the invention of the transistor, in 1949, came a new type of material called the semiconductor. It was found that semiconductors could meet the parametric needs far better than metals, and a new material, bismuth telluride (Bi_2Te_3) was developed and

found to have advantageous properties near room temperature. Also, because we typically operate a thermoelectric device thermally in parallel, and electronically in series, there is a necessity to have materials that transport heat in opposite directions with respect to current direction. Bi_2Te_3 is given the ability to be used for the two inversely related branches by doping it into extrinsic semiconductors. The electronic result of this process will be explained in a later section dedicated to material characteristics.

During the early research, great optimism was held for solid-state, environmentally friendly applications of the effect. Due to the state of materials sciences at the time, thermoelectric refrigeration and power generation efficiencies were significantly worse than their vapor-compression counterparts. Thermocouples, on the other hand, do not require efficient thermal to electric energy transformation. For this reason, they have been used and developed for much longer than TEG's and TEC's. As materials sciences advanced, increased efficiencies translated to using thermoelectric devices (TED's) in commercial and industrial applications requiring small dimensions, gravity independence, and a solid state/maintenance free design.

1.2.2 Self-assembly

The term "self-assembly" can be found referenced in many fields such as chemistry, physics, biology, mathematics and multiple disciplines of engineering. The definition used to describe the term varies widely between each field and has yet to be clearly and concretely stated to encompass all aspects of self-assembly. The definition, as described by Pelesko [14] caters well to engineering applications and is actually a conglomeration of various other definitions given in the past. It states that

“Self-assembly refers to the spontaneous formation of organized structures through stochastic process that involves pre-existing components, is reversible and can be controlled by proper design of the components, the environment, and the driving force.”

Typical forces harnessed for self-assembly include surface tension, capillary, magnetic, electrostatic, Van der Waals bond and gravitational [5].

Possibly driving the differences in the definition between fields, the reasons for studying self-assembly are also diverse. A simple reason is to understand the mechanisms that drive nature and life itself. Many biological processes are driven by chemical reactions that resemble microscopic manufacturing. From this, it is easy to see why the concept requires the attention of the chemist, biologist, physicist, engineer and more. By studying these basic interactions, the researcher strives to understand the systemic approach nature uses to efficiently and accurately build and maintain systems. Pertaining to engineering, self-assembly research finds use in building micro- and nanostructures. Also, smart materials, such as self healing materials, are being researched which utilize self-assembly concepts [6].

1.2.3 Thermal Haptics and the Thermal Grill Effect

The field of haptics is generally regarded as a study of how humans perceive the sense of touch. More specifically, this refers to kinesthetic, tactile and thermal feedback interaction which allows us to sense force, position, texture and temperature. Without haptic feedback, some of the most trivial tasks would be made nearly impossible and possibly dangerous to accomplish.

Human skin tissue has a variety of different types of sensors integrated within it, and with a combination of inputs, the brain is able to make judgments about object properties and structure. Temperature is sensed using two different types of nerve endings (receptors) which are found in the dermis [15]. Cold receptors are 30 times more abundant than their counterpart and also possess a quicker response due a difference in fiber material [16]. Furthermore, the sensory processing characteristics of these receptors should be understood to increase the effectiveness of the haptic device.

- (1) *Range* – Each receptor is dedicated to sensing cold or hot temperatures. The general range of neutrality for each type is from 30 °C to 36 °C where no sensation is realized. This region is also known as the “indifference zone.” [17] Again in general, painful sensations tend to dominate below 15 °C and above 48 °C. Haptic devices should perform within these ranges to provide safe, effective display of thermal information.
- (2) *Rate of change* – It has been realized that the thermal receptors in the skin largely detect changes in temperature (more specifically heat flux) versus absolute temperature of an environment. This is largely unique from the other modalities of sensation, i.e. vision, and within the indifference range, a person is even less apt to perceive slow changes in temperature.
- (3) *Resolution* – This property is very dependent on stimuli location, local skin temperature, and more, but the threshold of perception lies somewhere near 0.01 °C and is considered a relatively poor quality compared to other sensation types i.e. sight and hearing.

(4) *Spatial summation* – This refers to thermal receptors being more capable of determining intensity and interval of stimulation rather than spatially acute sensation. This drives some unique secondary characteristics, namely, the ability for a thermal threshold to be maintained while simultaneously decreasing the stimulus intensity and increasing the application area.

From these characteristics, it is determined human thermal receptors seem to act analogous to piezo (impulse) devices, versus having a sustained type of output like a thermometer. This realization is essential to designing a successful thermal display.

A related phenomenon known as the thermal grill and thermal illusion effect is also a consequence of the thermal receptors. This effect is defined as the perception of intense constant heating just under the threshold of pain that results from modulating heating and cooling on an area of skin. This effect was first discovered by Thunberg in 1896 [18]. There are various versions of the thermal illusion [19], and the terms synthetic heating and thermal grill illusion are often times used interchangeably. While the definitions of the two terms are not concrete, it has been generally accepted that thermal grill involves using hot and cold temperatures simultaneously, and synthetic heating uses only warm temperatures in a sequential manner.

Experimentation in haptics related to the thermal modality often employs use of a thermal display. A thermal display is defined as a device that is capable of conveying information to a human subject by means of applied heat [21]. Novelty in these devices comes in the form of the application of temperature or heat flux at the skin-device interface. TED's have been a popular choice in the design of thermal displays. The

advantages of using TED's include range of temperature, temperature control, size, solid state design and orientation independence.

1.3 Literature Review – Theory of the Thermoelectric Effect

There are three thermoelectric coefficients that have been defined for use with the thermoelectric effect. The differential Seebeck coefficient (α), also termed thermoelectric power, is defined as

$$\alpha_{AB} = \frac{V}{\Delta T} \quad (1)$$

where V is voltage potential and ΔT is the temperature difference between each junction. The Seebeck effect makes temperature measurement with a thermocouple possible. If two dissimilar metals are electrically connected and placed in environments with different temperatures, a measurable voltage potential will result, typically 1 to 100 $\mu\text{V}/^\circ\text{C}$ [7][8].

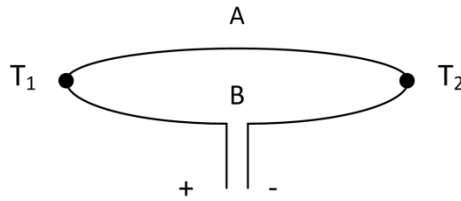


Figure 1 – Simple thermocouple design

The second defined coefficient is that of Peltier (π)

$$\pi_{AB} = \frac{q}{I} \quad (2)$$

where q is the ratio of the rate of heating or cooling at each junction to the electric current (I). It is demonstrated that the differential Seebeck coefficient is much easier to measure, and can be related to the Peltier coefficient by utilizing a Kelvin relation

$$\pi_{AB} = \alpha_{AB}T \quad (3)$$

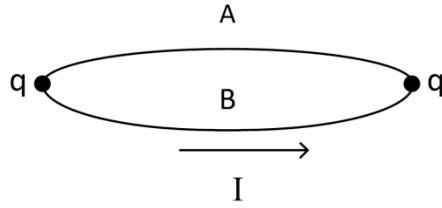


Figure 2 – A closed thermoelectric circuit. If materials A and B are different, a current will flow.

The final coefficient associated with the thermoelectric effect is the Thomson coefficient (τ), and is defined as

$$\tau = \frac{dq/dx}{I dT/dx} \quad (4)$$

It is important to note again that the Seebeck and Peltier coefficients can only be defined as a reference between two materials and are considered “surface properties,” and the Thomson coefficient is a bulk property of a single material [9]. Absolute Seebeck and Peltier coefficients can only be defined when a superconductor is used for one of the two materials. As stated before, it is acceptable to assume superconductors possess a Seebeck and Peltier coefficient of zero allowing an absolute value to be assigned to the second material. From this assumption it is also acceptable to relate the Thomson coefficient directly to an absolute Seebeck coefficient (S) by Equation (5).

$$\tau = T \frac{dS}{dT} \quad (5)$$

While these basic equations work well as material properties, a better way to describe actual thermoelectric performance has been determined. A dimensionless figure of merit relates multiple material properties known to influence the magnitude of the effect and is defined as,

$$ZT = \frac{S^2 T}{\rho \lambda} \quad (6)$$

where (λ) is defined as the materials thermal conductivity, and (ρ) is the electrical resistivity. Based on the figure of merit, it is traditionally accepted that a material with a high Seebeck coefficient, low electrical resistivity, and low thermal conductivity is a good thermoelectric performer. Also, these properties are all sensitive to the environments they are used in, so a high figure of merit at room temperature may degrade quickly as the temperatures stray in either direction. For this reason, specific types of thermocouples are to be used in very specific applications.

Shown in Figure 3, different types of elements are electrically connected in a configuration that cools at one side, and heats at the other. Typically, this pair of elements is repeated many times in a device to provide different physical dimensions and magnitudes of cooling power. Creating materials whose thermoelectric are inversely related to each other is discussed in the materials section of this chapter. In short though, semiconductors can be doped with other, property altering, materials to achieve this configuration.

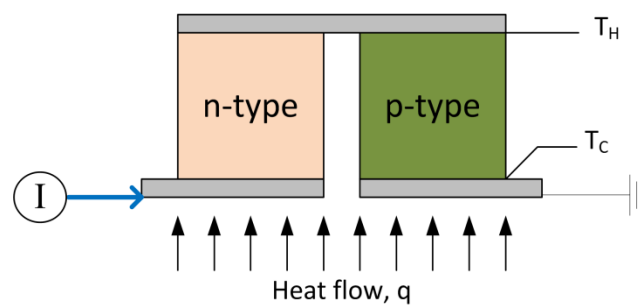


Figure 3 – Basic thermoelectric circuit

Assuming the material properties are temperature independent, there is no electrical contact resistance and heat flow is one-dimensional, the maximum achievable temperature difference between the hot and cold junction (T_H and T_C , respectively) is,

$$\Delta T_{max} = \frac{1}{2} Z T_C^2 \quad (7)$$

Because two different materials, possessing different properties, are now in use, a new effective figure of merit is defined to account for the inconsistencies between the two elements in Equation (8).

$$Z = \frac{(S_p - S_n)^2}{(\sqrt{\lambda_n \rho_n} + \sqrt{\lambda_p \rho_p})^2} \quad (8)$$

Basic conservation of energy equations have been derived for the hot and cold junctions using averaged material properties,

$$Q_H = K\Delta T - \frac{1}{2} J^2 R e - S J T_H \quad (9)$$

$$Q_C = S J T_C - \frac{1}{2} J^2 R e - K\Delta T \quad (10)$$

Where Q is the heat flux, J represents the current density, Re is the electrical resistance, K is the thermal conductance of the thermoelectric element and ΔT is the temperature difference between the hot and cold junctions. In Equation (9) & (10), $K\Delta T$ represents the heat conduction term, $1/2J^2R$ represents the effects of Joule heating, and SJT_H represents the thermoelectric effect. Because the current density term is squared, it is realized that the energy balance is very sensitive to changes in electric current. To maximize use of the effect, the electric current should be chosen in such a way that Joule heating does not dominate the energy equations. The use of this optimization can be seen

in Chapter 2 - Figure 9, where the heat flux increases to a maximum value, then starts to degrade as Joule heating begins to dominate.

The coefficient of performance (ϕ) of the thermoelectric model is defined as the amount of heat removed from the cold junction divided by the electric power input (P).

$$P = IV \quad (11)$$

$$\phi = \frac{Q_c}{P} \quad (12)$$

1.3.1 Materials

There are relatively few materials known to date that can be considered thermoelectric materials. Extrinsic semiconductor alloys have been shown to exhibit the best figures of merit since the mid-1900's with combinations of bismuth, antimony, tellurium and selenium being popular for low temperature use. Bismuth-telluride (Bi_2Te_3) is the most common combination and was used as the simulation material in this paper. In practice, this alloy would be doped, where impurity atoms would be diffused into interstitial sites, as well as interlayer sites. This was done with Ag and Cu, for example, to form n-type bismuth-telluride [10].

The use of the n-type and p-type is necessary for the following reasons. Materials that exhibit n-type behavior have impurities that donate electrons to the conduction band (Figure 4), hence they are called donors. The donors conduct electricity via quasi-free electrons. Conversely, p-type impurities act as acceptors of electrons and conduct through positively charged holes in the valence band [12]. With this, n-type and p-type materials can successfully be alternated in a device to provide heat pumping in the same direction.

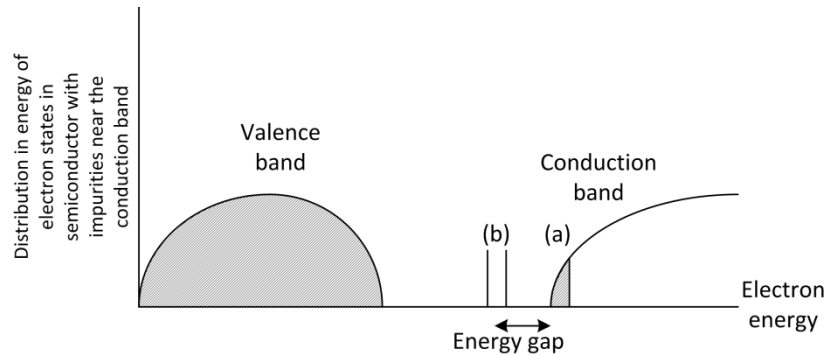


Figure 4 – Diagram of occupied electron states in a semiconductor with impurities. The conduction electrons (a) have been thermally excited from the donor impurity state (b) over the energy gap.

1.4 Thesis Outline

In the following chapter, FEA technique, application and results will be presented as they relate to the applications of self-assembly and haptics. Chapter 2 reviews the background and general technique of modeling coupled thermal-electric systems in the traditional Ansys FEA application. It also presents data to verify the accuracy of results against an accepted one-dimensional model. Using a model similar to that of the verification, Chapter 3 focuses on the performance of a micro-scale self-assembled device with assembly yields below 100%. The resulting performance characteristics are then discussed. Chapter 4 is a section written to demonstrate the design of a thermal haptic display utilizing thermoelectric macro-elements. FEA is used to predict the thermal characteristics of the device against skin. Finally, Chapter 5 is dedicated to recommendations for future research and final conclusions.

Chapter 2 – Three-dimensional FEA Analysis

Chapter 2 introduces a three-dimensional model for use in thermoelectric analysis at small size scales. Various Ansys mesh element types are explored for this application in addition to some newly introduced characteristics relevant to small size-scales and typical system designs. A batch program is also described which automates the creation, solution, and display of results for the model. From this data, a comparison is made to a published one-dimensional model to determine accuracy and applicability to future analyses.

2.1 Three-dimensional Thermoelectric Modeling in Ansys v12.1

Ansys v12.1 (Traditional) was used to model a thermoelectric device in three-dimensions. Because devices are typically powered electrically in series, one-dimensional analysis is sufficient to predict basic performance characteristics such as T_C , T_H and Q_C . When analyzing a self-assembly process, however, multiple same-type elements are often designed to be assembled in parallel groups to increase the probability that a closed circuit is created during the self assembly process. Adding parallel groups is termed adding a redundancy factor (R). Because assembly yield rates are expected to be less than 100%, each cluster of n- and p-type elements could be composed of a different number of elements. For this case, three-dimensional FEA should be used to model the various thermal and electrical inconsistencies of the system. Consider a system with a

redundancy of 4. If the number of successful assemblies in a particular group is less than 4, the current density through that group will increase by 33%, 100%, and 300% for a group with 3, 2, 1 elements successfully assembled, respectively. With current densities varying so much, performance characteristics of the device will also vary accordingly. This is the major reason for analyzing devices in more than one or two dimensions.

Ansys v12.1 [27] has included three element types to handle thermal-electric systems. PLANE223 is a 2D 8-node quadrilateral which can be degenerated to a 6-node triangle as well as made to have unit thickness associated. SOLID226 is a 3D 20-node hexahedron (brick) element. SOLID226 was chosen to represent thermoelectric material in this works model. SOLID227 is a 3D element that has configurations including a 10-node tetrahedron, 13-node pyramid, and 15-node prism. SOLID227 was applied to the copper contact volumes as a 10-node tetrahedron which made the mesh interface between thermoelectric element and electrical contact couple nodes better. This is important because the thermal and/or electrical information at the unmatched nodes will hit a dead-end and be lost which introduces inaccuracies into the solution.

In the calculation of a solution, the thermal load vector depends on the result of a separate electric solution at each node. This causes the solution to be non-linear for steady-state and transient systems, and requires at least two iterations to achieve convergence. For each unconstrained node, the solution produces a temperature and electric potential. Reactions, such as heat flow rates, and electric currents also occur in correctly constrained nodes as a result of the solution. From each nodal solution, elemental Joule heating, current density and heat flux are determined [27].

The model presented uses the SOLID226 element type for the thermoelectric n- and p-type material, and SOLID227 for the electrical contact strips. The SOLID226 brick elements are set to be one-sixth the height of the thermoelectric element. Smaller mesh sizes were attempted; however the maximum number of nodes supported by Ansys v12.1 was exceeded. This element size was tested and shown to be sufficient in the following section. Furthermore, heat transfer from the side walls of the elements is neglected. This side wall assumption could easily be adjusted by adding a conducting medium between the side walls as seen in research by Ziolkoski [36], but it is not accounted for in the analytical model and is not thought to have a significant impact on the final solution in this analysis. The properties assigned to the two thermoelectric materials were averaged values of the Seebeck coefficient, thermal conductivity and electrical resistivity and are seen in Table 2. In the analysis of a true three dimensional system, these values should not be averaged, but as this model was compared with a one-dimensional model which does use averaged values, the same properties were used. Similarly sized SOLID227 tetrahedral elements are used for the contact straps. These are given properties typical of a copper conductor. The two properties assigned to this material were thermal conductivity and electrical resistivity.

Specifically, this model is based on a generalized system described in detail in Miner [35]. The basic system is described by including entry and exit substrates with corresponding thermal conductances (K_{CE}/K_{HE}). Also, source and sink temperatures (T_S and T_A , respectively) are applied to better simulate the true application of a thermoelectric device. The original use of this technique was to predict the performance of devices as size scales were reduced and contributions from components like contact

resistance were magnified. This method also accounts for how heat is delivered and sent to and from each junction, which better predicts actual junction temperatures (T_H and T_C). A fill factor (f) is also introduced, which serves to illustrate the effects of a given ratio of thermoelectrically active area to the entire cooler area. In this model, the fill factor is used to control geometry, but its usefulness can be extended if sidewall conduction through a fill medium is to be added to the model. Used at micro and nano-scales, this factor can have a significant effect on the degradation of the figure of merit by adding to thermal interface resistances.

Seen in Figure 5, dimension L_f is a function of the fill factor, the total number of elements (N) and element length (L_e) and can be calculated by,

$$L_f = \frac{NL_e \left(\frac{1}{\sqrt{f}} - 1 \right)}{N - 1} \quad (13)$$

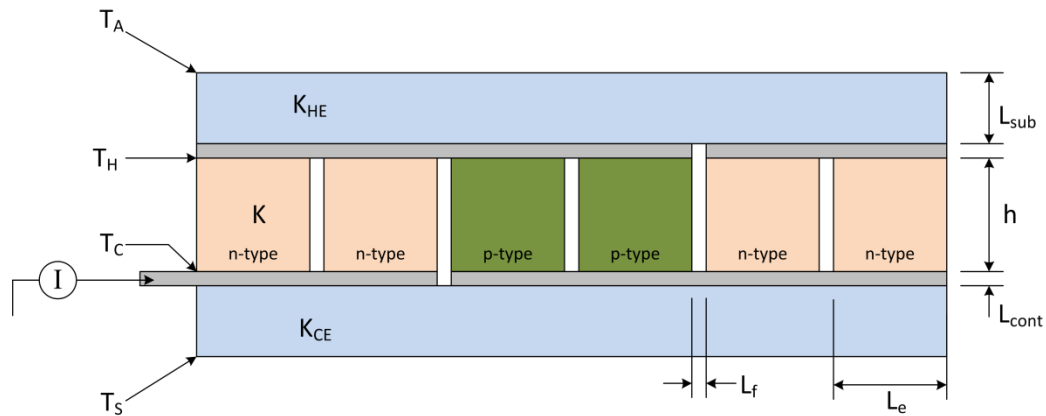


Figure 5 – Design schematic of 6x6 array with a redundancy of 4.

Table 1 – Characteristic dimensions for a 6x6 array with a fill factor of 0.9

Model Dimensions			
L_{sub} (*10 ⁻⁴ m)	L_e (*10 ⁻⁴ m)	L_{cont} (*10 ⁻⁴ m)	L_f (*10 ⁻⁴ m)
1.7500	2.0000	0.2500	0.1298

The substrates used to model entry and exit thermal conductance paths are considered to be electrical insulators but are assigned a thermal conductivity. Considering the scale of model, the thermal contact resistance was included in the conductivity of the substrate. Using Equations (17) and (18), K_{CE} and K_{HE} were determined and used to find the corresponding equivalent thermal conductivities (k_{sub}) for use in Ansys.

$$k_{sub(CE)} = L_{sub}K_{CE} \quad (14)$$

$$k_{sub(HE)} = L_{sub}K_{HE} \quad (15)$$

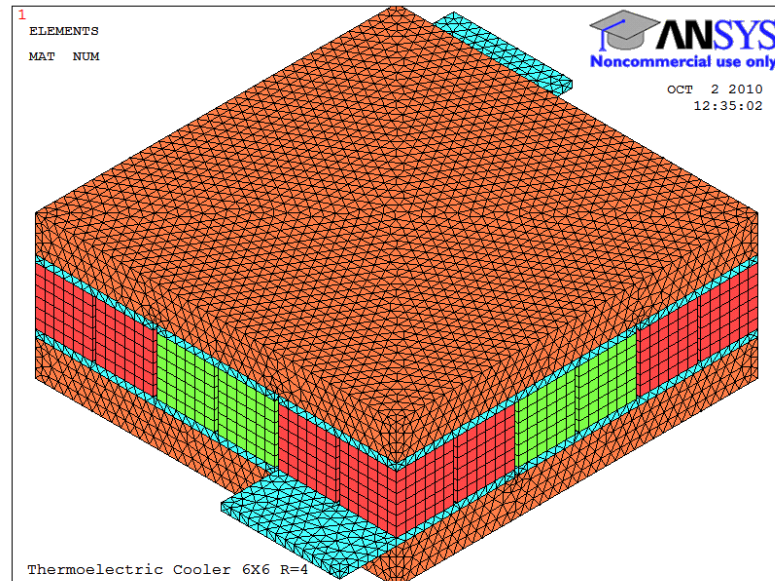


Figure 6 – 3D Mesh of a 6x6 thermoelectric cooler with a redundancy of 4.

The boundary conditions for the system include thermal and electrical components. There is a defined beginning and end for the current path. Based on the desired direction of heat pumping for the thermoelectric elements, a current vector is applied to one end of the simulated device. The magnitude of the current vector is calculated from a given current density and is a function of the cross-sectional area of a

fully assembled group of elements. The optimal current density for a set of given boundary conditions is determined analytically in the one-dimensional model and manually input into the Ansys batch code. The thermal boundary conditions applied are a source temperature, T_S , on the side of the cold junction, and a sink (or ambient) temperature, T_A , on the side of the hot junction (see Figure 5). These two temperatures are applied by coupling the nodes of the entire surface on the respective sides of the substrate.

Table 2 – System properties for Bi₂Te₃ based analysis

	$S (*10^{-6})$ (V/K)	λ (W/mK)	$\rho (*10^{-5})$ (Ω -m)	<i>Element type</i>	<i>Element features</i>
<i>n-type Bi₂Te₃</i>	-240	2	1	SOLID226	Thermal-electric
<i>p-type Bi₂Te₃</i>	240	2	1	SOLID226	Thermal-electric
<i>Copper contacts</i>	-	400	0.0017	SOLID227	Thermal-electric
<i>Substrate</i>	-	2.21	-	SOLID87	Thermal

A batch program was written for use in Ansys (Appendix A.1) which allows quick and automated creation and solving of the thermoelectric system described. The code was written to give the user control of various system parameters. One of the main goals of this project was to make the code flexible enough for use in the future study of self assembled TEC's. Some of the important easily modifiable parameters include material properties (S , λ , ρ), element height, element length/width, substrate thickness, current density and boundary temperatures. Also, seen in the following section is a methodology used to include thermal contact resistances in the substrate conductivity. This scheme was integrated into the calculation of equivalent substrate conductivities.

Also, Equation (13) was developed to be used in the code to automatically calculate element spacing based on the assigned fill factor.

2.2 Verification of the Ansys Model against Generalized Thermoelectric System Theory

Recent work has produced a more accurate depiction of small scale TEC's by introducing non-ideal conditions of thermal contact resistance, substrate conductance and parasitic heat paths [35]. As element length is scaled down to a range of 50 μm to 500 μm [29]-[32], it is expected the thermoelectric performance will be near its best and is where methods of micro-manufacturing techniques are currently being researched [34]. In his one-dimensional model, Miner [35] defines a number of updated equations to include these effects. An equivalent thermal substrate conductance is defined which accounts for element density, contact resistance, and the ratio of thermoelectric element conductivity to contact conductivity (g). It is noted that there is limited data to define a value for g , and this study uses a value of 0.1 mm based on its use in other work [29]. The new entry and exit substrate conductance (K_{CE} and K_{HE} , respectively) can then be added to the energy balance as seen in Equations (19) and (20). These equations describe the generalized thermoelectric system seen in Figure 7.

$$K^* = \frac{k}{g} \quad (16)$$

$$K_{CE} = \frac{K^* K_C f}{K_C g + K^* f} \quad (17)$$

$$K_{HE} = \frac{K^* K_H f}{K_H g + K^* f} \quad (18)$$

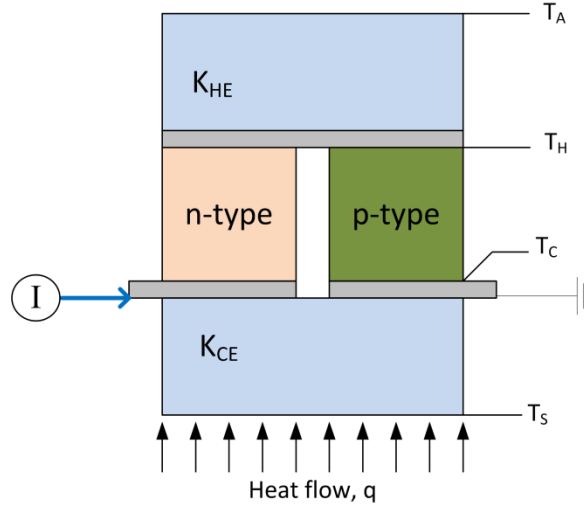


Figure 7 – Simple generalized thermoelectric system.

In this system, the two boundaries, T_S and T_A are constrained to a constant value. The entry conductance region lies between the source temperature and cold junction, and the exit conductance region lies between the hot junction and the ambient environment.

$$(T_A - T_H)K_{HE} + JST_H + (T_C - T_H)K + \frac{1}{2}J^2R = 0 \quad (19)$$

$$(T_H - T_C)K + \frac{1}{2}J^2R - JST_C + (T_S - T_C)K_{CE} = 0 \quad (20)$$

This one-dimensional general system model was run for a variety of conditions and compared to an equivalent three-dimensional Ansys model to compare the calculated cold-side temperature, hot-side temperature and cold side heat flux. Using the modeling techniques in Chapter 2.1, the three-dimensional model was designed to be equivalent to the one-dimensional case. The thermal contact resistance of the one-dimensional model was found to have a large impact on the solution. For this reason it was necessary to also include the effect in the three-dimensional case. This was successfully accomplished by deriving equivalent substrate conductivities by using the following scheme:

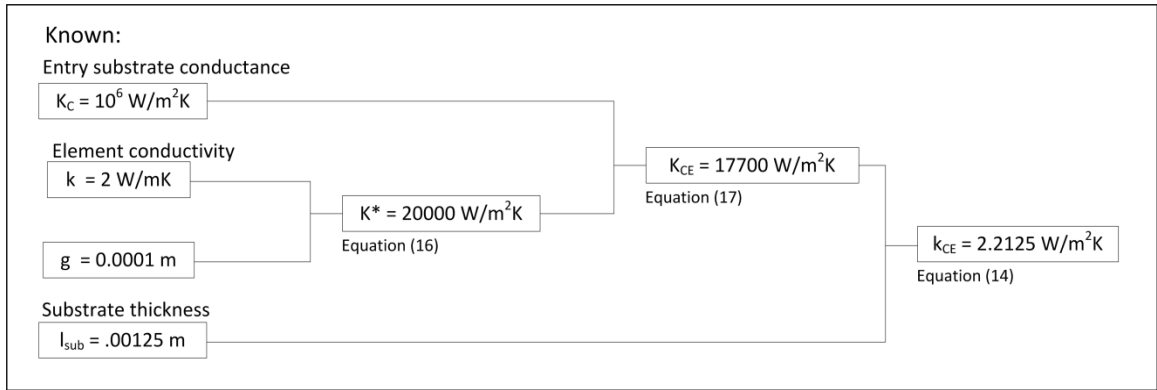


Figure 8 – Methodology for equating entry substrate conductance to an equivalent conductivity that includes thermal contact resistance.

Figure 9 shows the case where T_S and T_A are held constant, and the current density (J) is varied from 0 A/m^2 to $2.5 \times 10^7 \text{ A/m}^2$. It can be seen that while there is near perfect agreement with T_C and T_H , there is a small deviation in the calculated heat flux. The maximum error of Q_C was found to be 7%, or 0.76 W/cm^2 , at $1.25 \times 10^7 \text{ A/m}^2$.

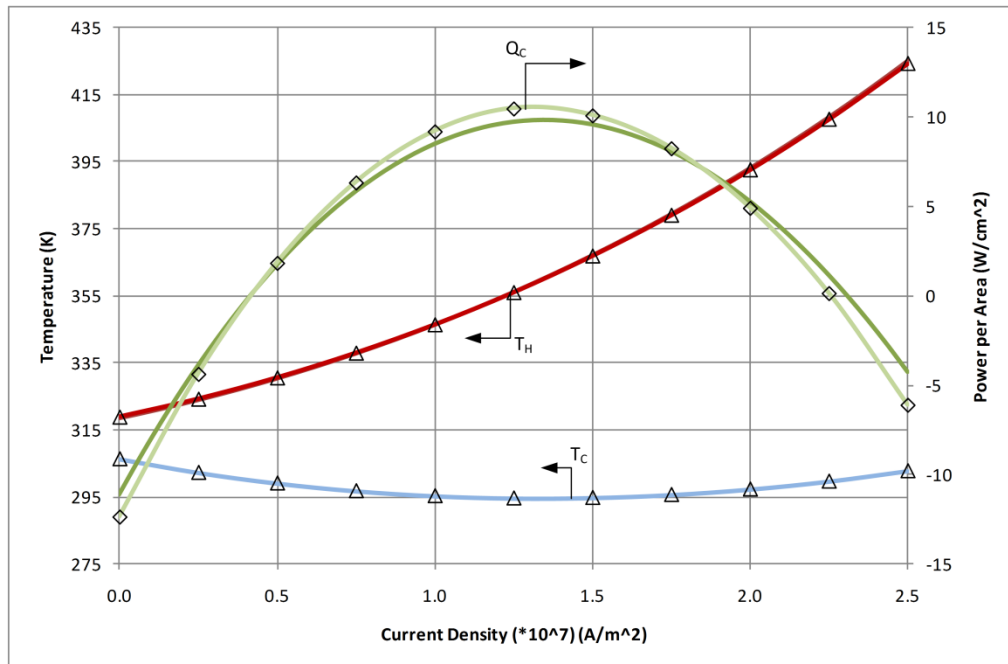
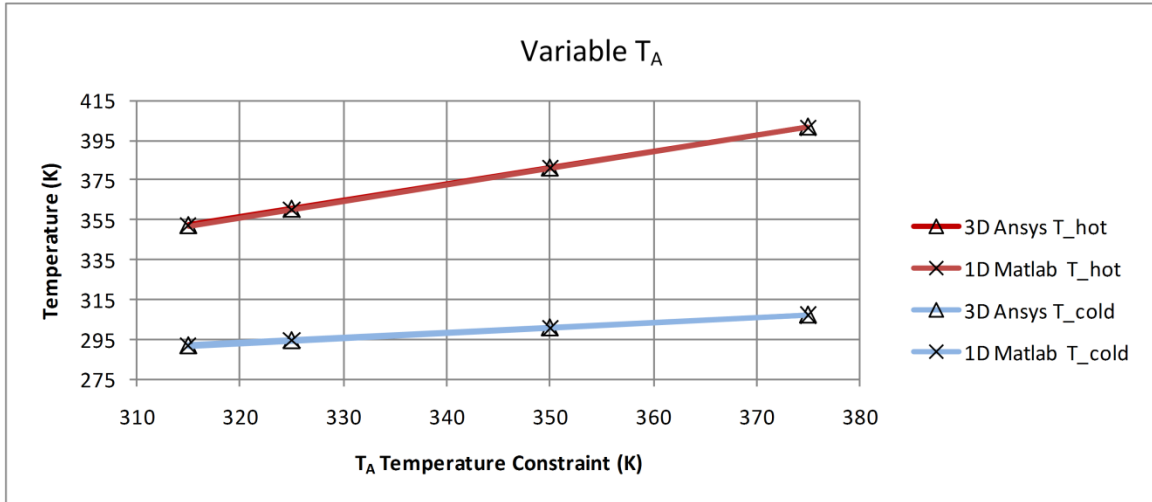
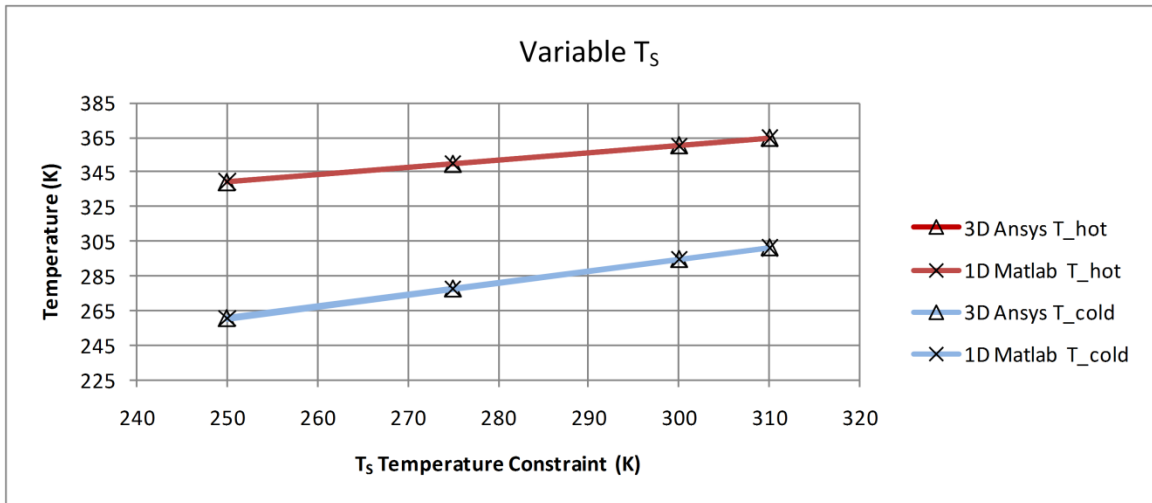


Figure 9 – Plot of analytical and FEA solutions of thermoelectric performance with constant boundary temperatures T_S and T_A and varied current input. Ansys results are shown with discrete points and the analytical solution is shown as a smooth curve.

The model was also tested using fluctuating boundary temperatures. In this test, the optimized current for a particular combination of T_S and T_A was extracted from the analytical one-dimensional model and manually input into the Ansys code. For the first set of boundary conditions, T_S was held at 300 K, while T_A varied from 315 to 375 K. In the second set of boundary conditions, T_A was held at 325 K and T_S varied from 250 to 310 K. Shown in Figure 10, the temperatures compared well and deviations between the two models were of the order of 0.2 K for the entire range of boundary conditions. These values were accepted and considered to be in agreement. In addition, as Q_C was compared while using the optimized current condition, better correlation was seen between the analytical and numerical models. This agreement indicates models run with optimized parameters will result in more accurate solutions. The maximum error observed in this analysis was 0.47 W/cm^2 when T_A is equal to 325 K and T_S is equal to 310 K.



(a)



(b)

Figure 10 – Temperature plots for varying boundary temperatures where (a) T_S is held constant and T_A varies from 315 K to 375 K, and (b) T_A is held constant and T_S varies from 250 K to 310 K.

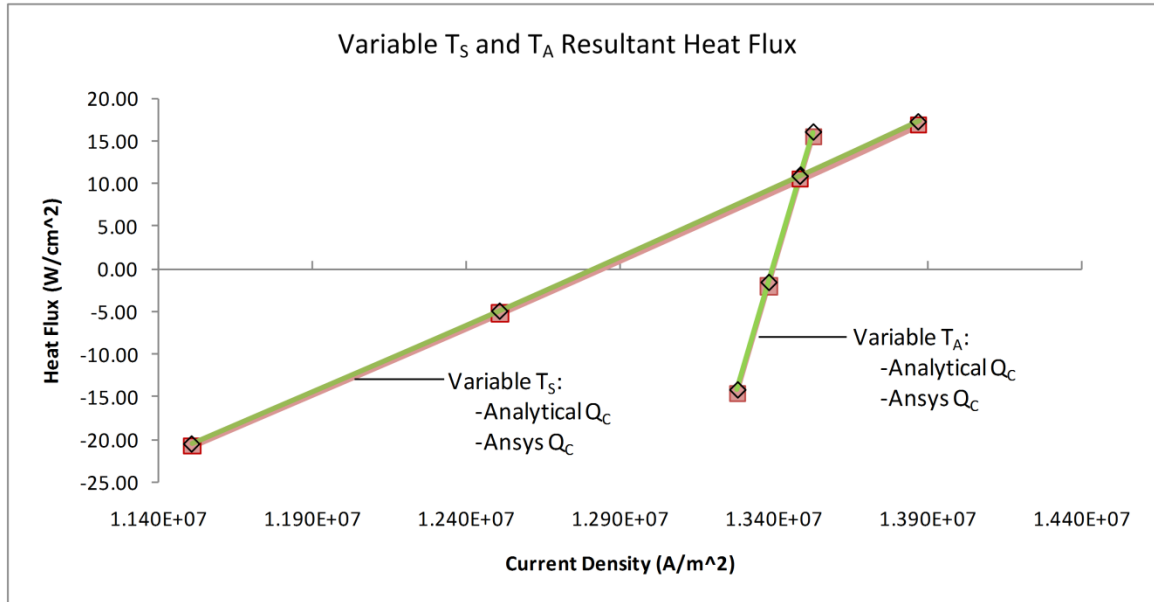


Figure 11 – Comparison of heat flux at the cold-side junction under conditions of varying T_A and T_S.

It was concluded that the three-dimensional Ansys model compared sufficiently well with the one-dimensional analytical simulation. With this acknowledgment, three-dimensional systems of self assembled elements will be analyzed in confidence using the same modeling approaches used in the verification.

Chapter 3 - Analysis of Three-dimensional Self-assembled Devices

Chapter 3 is meant to employ the three-dimensional model described and verified in Chapter 2. The application of self-assembled thermoelectric devices is introduced in this chapter where the concept of redundant electric paths is described and modeled using parallel n-type or p-type elements in clusters. Multiple cases of less than ideal yield configurations are presented and simulated in Ansys v12.1. Thermal performance of the subsequent system is then analyzed and discussed to determine the impact of having vacant element sites within a device.

3.1 Description of the Three-dimensional Finite Element System

In the analysis of a TEC in three dimensions, a section of a fully assembled device is modeled to show the local affects of missing or nonfunctional elements. This is done to decrease the simulation time and allow for a higher node density in the academic version of Ansys v12.1. In these analyses, a 6x6 array of thermoelectric elements with redundant same type element clusters of 4 are modeled under various non-homogeneous configurations. In Ansys, discrete volumes are defined by assigning values ranging from 1 to 36. Figure 12 shows the location of each volume, and is referenced to describe which elements are thermally and electrically active. Element 9-12 are defined as the center cluster, and the group of clusters surrounding this are defined as edge clusters.

Like the verification model, a one dimensional Matlab model was used to determine the optimal current density for a given system of properties and boundary conditions. This system configuration, given in Table 3, was considered the basis for each of the Ansys analyses for comparison.

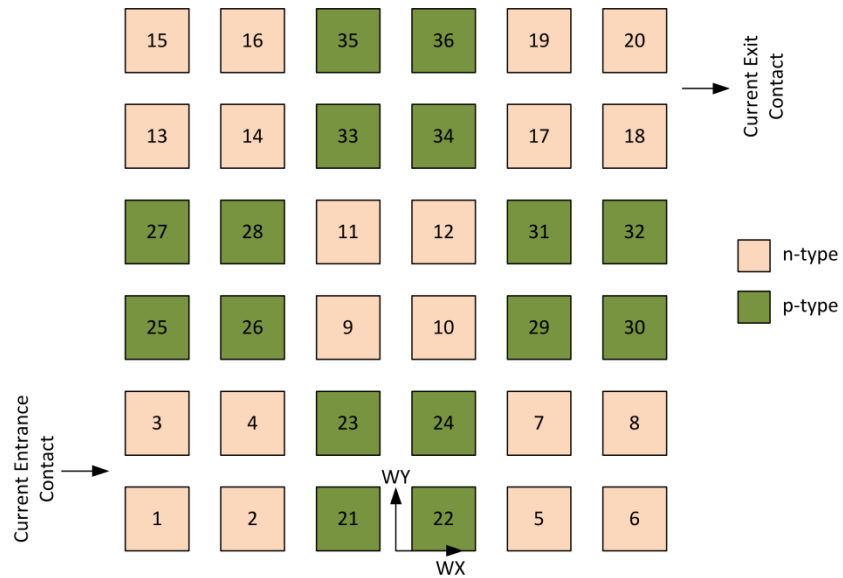


Figure 12 – Assigned thermoelectric volume numbers and locations for a 6x6 array and redundancy of 4. Figure orientation is based on the default workplane directions and entrance and exit current paths.

Table 3 – Key system properties and parameters used in the analysis of a three dimensional thermoelectric device

Element Parameters					
<i>Thickness</i> <i>(m)</i>	<i>Resistivity</i> <i>(Ω-m)</i>	<i>Thermal</i> <i>Conductivity</i> <i>(W/mK)</i>	<i>Seebeck</i> <i>Coefficient</i> <i>(μV/K)</i>	<i>Fill Factor</i>	<i>Redundancy</i>
2.00E-04	1.00E-05	2.0	240	0.9	4

Substrate Parameters		Contact Parameters		
<i>Thickness</i> <i>(m)</i>	<i>Thermal</i> <i>Conductivity</i> <i>(W/mK)</i>	<i>Thickness</i> <i>(m)</i>	<i>Resistivity</i> <i>(Ω-m)</i>	<i>Thermal</i> <i>Conductivity</i> <i>(W/mK)</i>
1.25E-04	2.2125	2.50E-05	1.70E-08	400

Boundary Conditions		
<i>Source</i> <i>Temperature</i> <i>(K)</i>	<i>Sink/Ambient</i> <i>Temperature</i> <i>(K)</i>	<i>Current</i> <i>Density</i> <i>(A/m²)</i>
300	325	1.3485E+07

The impact of missing elements was assessed by comparing the heat flux and temperature profiles with different number of elements. Figure 13 shows the paths on which the temperature profiles are measured. Figure 14 shows the temperature profile through Path B and Path C for the fully assembled system. Path A is assumed to be equal to Path B in the fully assembled system.

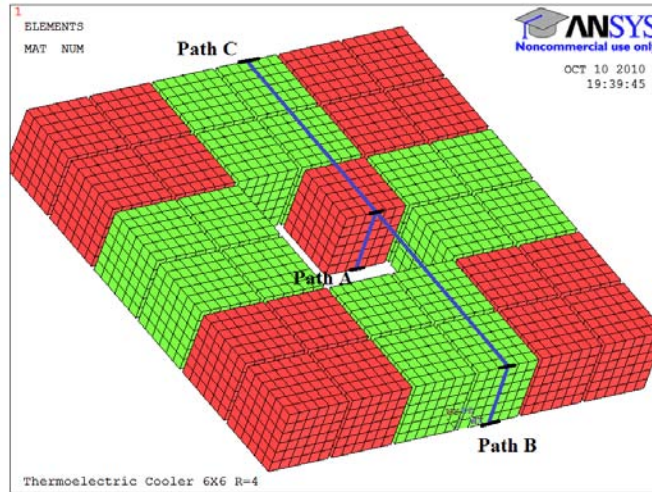


Figure 13 – Description of the paths for temperature profile plots

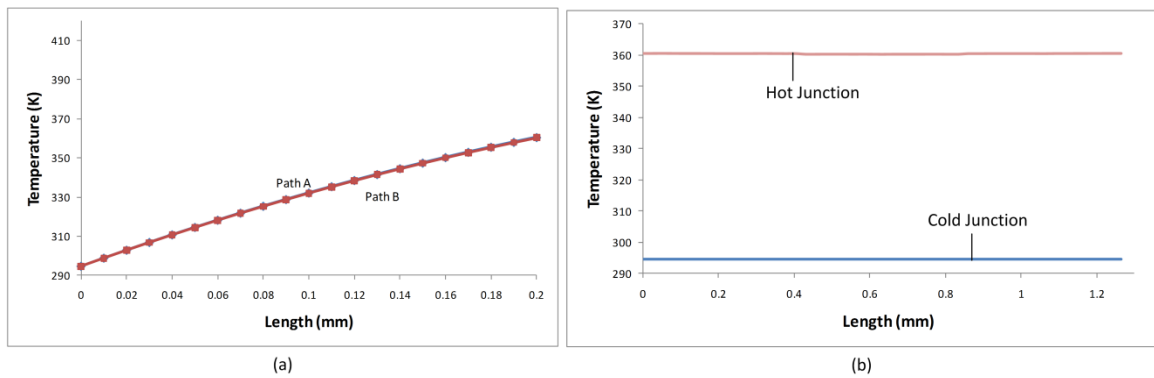


Figure 14 – Temperature profiles plotted along (a) Path A and Path B, and (b) Path C at the hot and cold sides.

The temperature profiles in Figure 14 describe a system where each cluster is performing equally. This is expected considering the current magnitude is the equal throughout the model, and geometric symmetry exists in multiple directions.

3.2 Self-assembled Configurations of Missing, Centrally Located Elements

Three cases of functional systems containing less than ideal assembly yields were simulated under the same conditions stated in Section 3.1. The purpose of the analysis was to determine how vacant assembly sites would affect the overall performance of a TEC as well as look at the local thermal effects on the remaining elements in the cluster. The solutions of these cases are used to determine whether or not a particular configuration would remain useful and acceptable. While there are many characteristics that could be chosen to determine acceptability of a device, it is believed that two good indicators of system performance are T_C and Q_C . As current is increased, T_C will decrease until Joule heating causes a parasitic heat flow in the direction opposite of heat pumping. This will also cause a reduction of the net heat flux at the cold-side junction which is undesirable. With access to the nodal temperatures at any point in the three-dimensional model, new methods are presented to describe system performance and acceptability, specifically how the temperature profiles differ within a single model, as well as how the edge clusters performances are affected compared to the 100% assembly yield case.

Below, in Figure 15, the three cases are presented in two-dimensions to show the locations of vacant assembly sites. Center elements were chosen to simulate the case where elements were missing in the interior of a much larger array. Local thermal effects were not expected to spread past the edge clusters.



(a)



(b)



(c)



(d)

Figure 15 – (a) Control case with full assembly (b) Case 1 with one center element missing, (c) Case 2 with two center elements missing, (d) Case 3 with three center elements missing.

3.3 Review of Results from Three-dimensional Ansys Analyses

Results of the three previously described cases were obtained and analyzed to determine total and local thermoelectric performance. Nodal data extracted from Ansys included total heat flux from the cold reservoir (Q_C), local values of T_H , local values of T_C , and the temperature profiles along the previously defined paths. This data provided a detailed representation of thermoelectric performance.

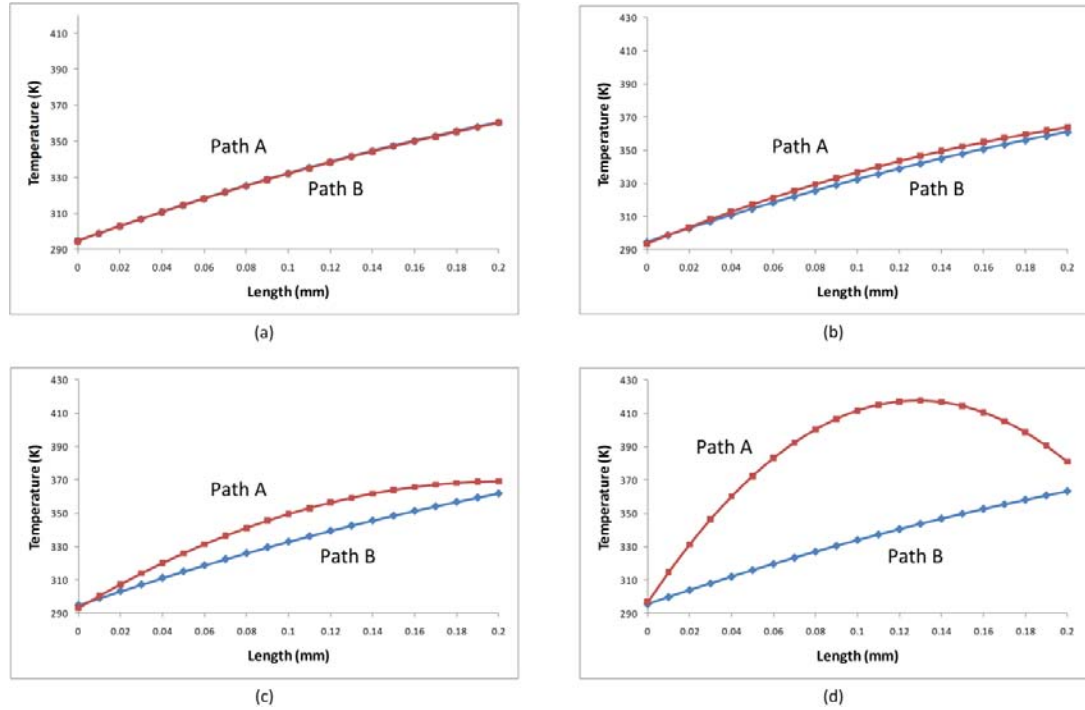


Figure 16 – Path A and Path B temperature profiles for (a) the fully assembled control case, (b) one central missing element, (c) two central missing elements, and (d) three central missing elements.

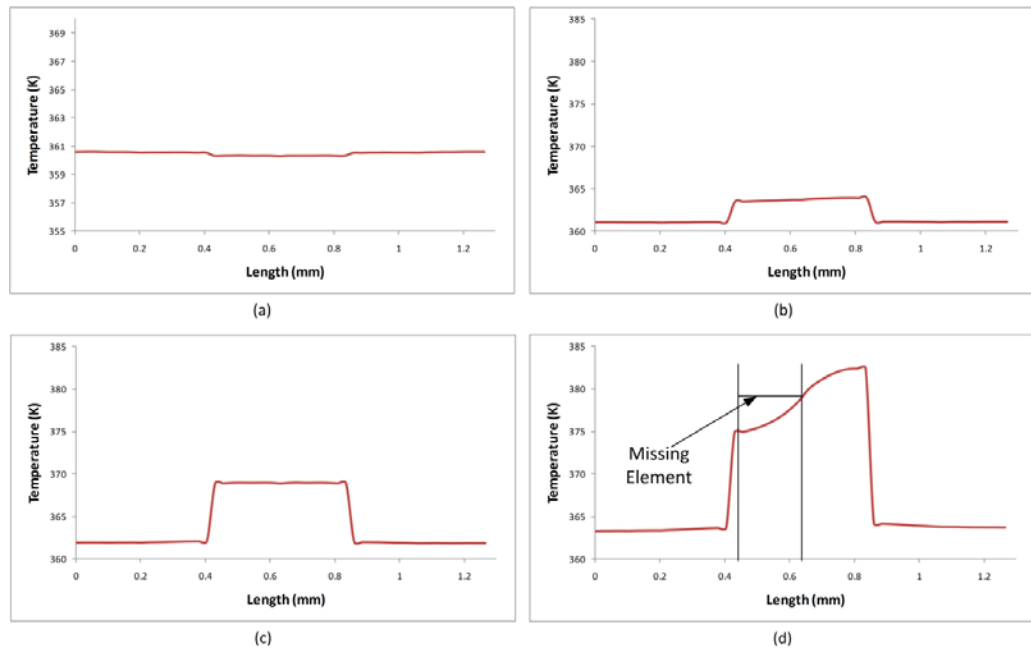


Figure 17 – Path C temperature profiles along the hot-side junction surface (a) for a fully assembled case, (b) with one central element missing, (c) two central elements missing, and (d) three central elements missing.

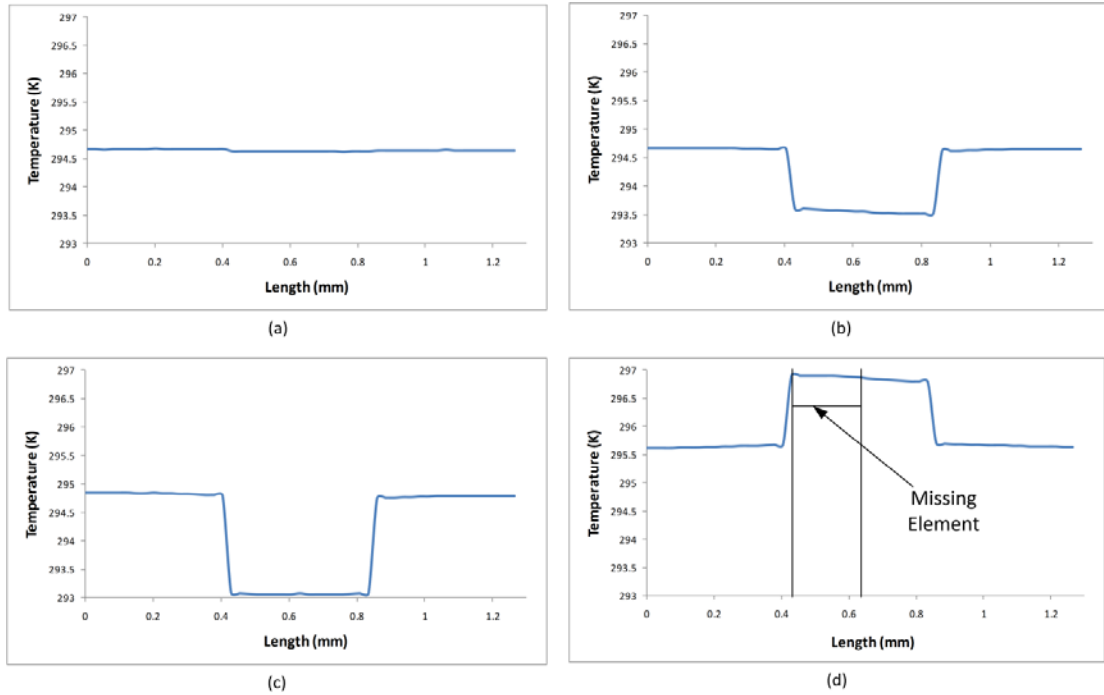


Figure 18 – Path C temperature profiles along the cold-side junction surface (a) for a fully assembled case, (b) with one central element missing, (c) two central elements missing, and (d) three central elements missing.

Table 4 – Results extracted from the Ansys solution for traditional performance analysis. The listed junction temperatures are seen in the center cluster.

FEA Results from Ansys				
Vacant sites	T_C (K)	T_H (K)	q_c (W)	Q_c (W/cm ²)
0	294.67	360.53	0.1508	10.47222
1	293.50	363.96	0.15311	10.93643
2	293.14	370.68	0.14796	10.87941
3	295.43	417.72	0.1079	8.174242

3.4 Discussion of Results

Two things can happen as elements become nonfunctional in a cluster and the current magnitude increases through the remaining elements: In some cases, the local thermal performance will actually increase or remain relatively unchanged from a

completely assembled cluster. That is, T_C will decrease, T_H increases, and Q_C increases which corresponds to an increase thermal of performance. Second, the thermal performance can degrade as current magnitude increases and Joule heating dominates causing a parasitic heat flow. This causes an increase in T_C , T_H , and Q_C and ultimately, a decrease in overall performance

The plot of Path A in Figure 16 represents the internal temperature gradient present within the remaining center elements. With the removal of each element, the temperature profile of the center elements become less linear as the magnitude of Joule heating increases. From a design standpoint, any energy loss due to Joule heating is undesirable because it is a non-reversible process and does not improve heat transport, but it is an effect that is unavoidable. In the extreme case where only one of four elements is successfully assembled, the current is 300% greater than the edge clusters and the internal temperature of the element rises drastically to a maximum value of 417.7 K. The other cases, shown in plot (b) and (c) of Figure 16, show maximum temperatures at the hot junction of 363.9 K and 269.2 K, respectively. Also, the total system heat flux with one element missing rose 0.46 W/cm^2 and with two elements missing rose 0.40 W/cm^2 compared to the fully assembled case. Although the temperature curves of (b) and (c) become less linear, the thermal performance at these two conditions is shown to actually increase. This is thought to be the result of a more optimal fill factor condition being found as empty space increases in the center cluster. This was further proven by removing one element from each cluster, thus making it an R=3 system with a fill factor equivalent to 0.675, and solving the system with the same boundary conditions used prior. The results shown in Table 5 show that, although the thermal performance

increases for systems with R=3 and R=2, the coefficient of performance decreases in each case. This means that the input current is not ideal for the conditions, but if the efficient use of power is not of concern, this can be overlooked. In future models, accounting for optimal fill factor could have a significant impact on increasing device performance.

Table 5 – Performance and efficiency comparison between closely packed elements verses less closely packed elements under equal boundary conditions.

FEA Results from Ansys								
	T_c (K)	T_H (K)	q_c (W)	Q_c (W/cm ²)	I (A)	V (V)	P (W)	ϕ
R=4	294.7	360.5	0.1508	10.47	2.1576	0.396	0.85	0.177
R=3	293.3	371.4	0.1815	16.81	2.1576	0.500	1.08	0.168
R=2	292.5	386.0	0.1762	16.31	2.1576	0.694	1.50	0.118
R=1	303.4	451.1	-0.083	-7.70	2.1576	1.245	2.69	-0.03

Further analysis was done on Figure 17 and Figure 18. Here, the difference in temperature between the center elements and edge elements is clearly seen. The average difference for the hot/cold sides was found to be 2.4/1.1 K, 6.9/1.7 K and 10.9/-1.1 K, for (b), (c) and (d), respectively. This shows that the hot side junction is much more sensitive to changes in current magnitude. On plot (b) for both figures, a slight variation in temperature can be seen across element volume 10. This is thought to be a result of the vacant site located next to it not providing the conducting heat energy needed to maintain the elevated temperature. Also, for plot (d), an elevated temperature is seen where there should be an element missing. This happens because the measurement path lies directly in between the element top surface and the copper contact bottom surface. With this realization it was concluded that the temperatures plotted are from the bottom side

contact surface. The slope of the temperature gradient in this area is due to conducting heat from surrounding elements.

From the given data it was concluded the case with three missing elements does not display characteristics of an acceptable TEC. The performance of the cases with one and two missing elements, however, only deviated from a fully assembled system marginally. For applications where the main control parameter is net heat flux, case (b) and (c) would be considered acceptable considering this performance increased. In an application where temperature uniformity of the hot or cold junction was the main concern, case by case analysis would have to be done to justify acceptability.

Chapter 4 – Haptic Thermal Display

Chapter 4 presents a project related to the field of haptics focused on the design of a thermal display built to test the thermal grill illusion. Design requirements for the display are described and lay out a framework for a prototype design. The prototype design uses five independently controlled rows of thermoelectric elements and is built to be affixed to the forearm of a test subject. Finally, static FEA is done to characterize the thermal performance of the device against human skin tissue at multiple time-steps during simulated application of the thermal grill illusion.

4.1 Design Requirements

When designing a thermal display, certain key features must be included. Possibly the most fundamental and important is control. In order to quantify an experimental response, the tester must be able to control the inputs given to the subject during an experiment. In this project, it is important to control the skin side temperature of the device accurately and quickly. Based on literature [37], the applied temperature combinations for use displaying the thermal grill illusion vary from different sources. Non-painful display of the effect was observed with various mild temperature combinations of cold (31-26 °C) and warm (35-40 °C) [38]. Secondly, critical temperatures need to be established to prevent injury to the test subject. It has been established in previous studies [16] that the average thermal pain thresholds are near 45

°C for warm temperatures, and near 15 °C for cool temperatures. With this in mind, the control device should be capable of performing an emergency cutoff if skin side temperatures approach the pain threshold limits.

How the temperature gradients are presented to the skin is also of importance. The designated area of experimentation will be on the outside (dorsal) or inside (ventral) of the forearm, where surface geometry, specifically rate of curvature, can vary widely between individuals. For this reason, the device should be made flexible to conform to different curved surfaces. Also, a means of comfortably attaching the device to the forearm is necessary. The device and components should be held securely to the arm while not obscuring the ability to sense changes in temperature with kinesthetic interaction.

4.2 Design and Components Used

The thermal feedback display presented in this paper consists of five discretely controlled rows of thermoelectric elements. Each independent row is made up of 4 elements connected electrically in series, and thermally in parallel by using n-type and p-type Bi₂Te₃ based material. The distance between each row is 0.4 inches

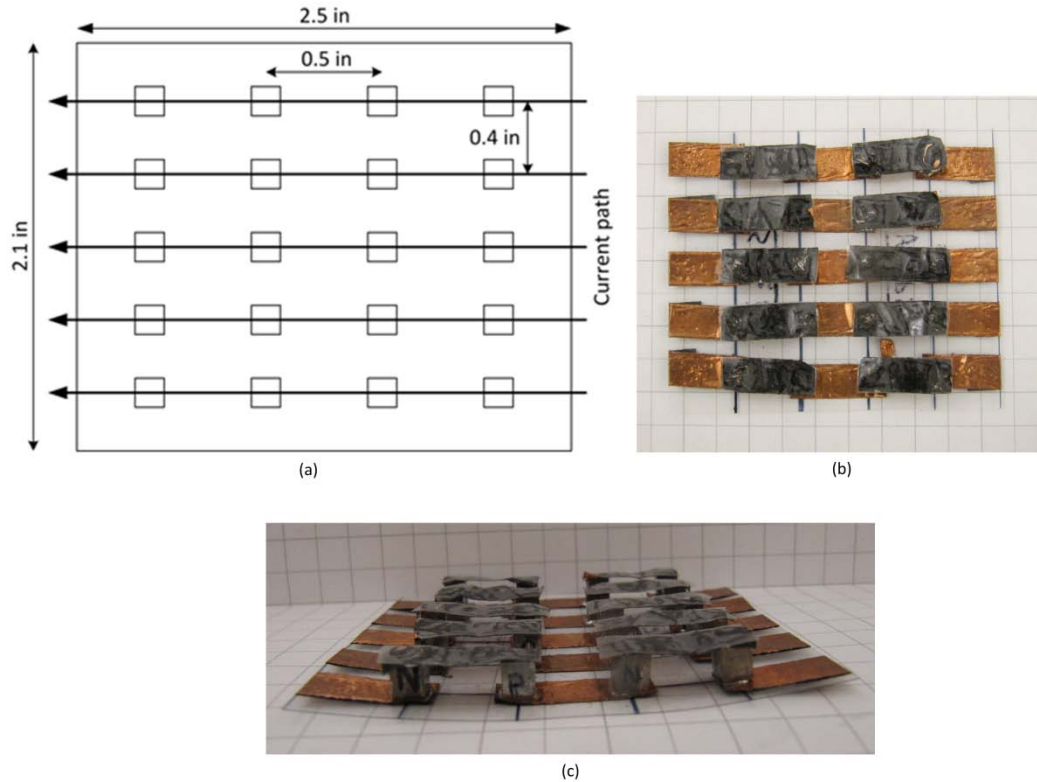


Figure 19 – (a) Schematic of thermoelectric array with discretely controlled element rows, (b) Top view of the display, (c) Side-view of the thermal display

The thermoelectric elements have dimensions of 3.8 X 3.8 X 4.8 mm, where 4.8 mm is considered the element height. For each independent row, copper tape was used as the electrical contact material between elements. The copper tape has an adhesive backing that attaches to the substrate, and is soldered to each element on the copper side as seen in Figure 20. The spacing between each element is thought to have an impact on how thermal information is perceived. For this reason, each row was kept a distance of 0.4” apart. This should allow each row to be perceived separately while still exhibiting the spatial summation needed to experience the thermal grill illusion.

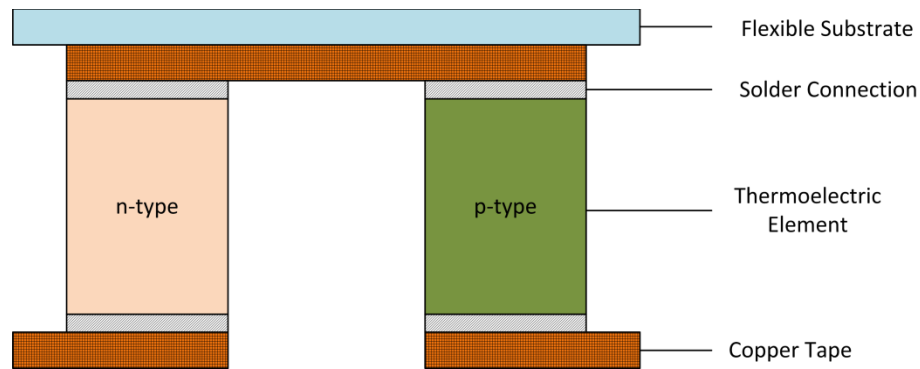


Figure 20 – Design section for a proposed thermal display.

Flexibility was accomplished by using a thin vinyl film (2.5” x 2.1” x 0.004”) as a substrate on the display side. The substrate acts to retain geometric dimensions of each row, as well as provide protection from electric shock as currents up to 4 Amperes could be used during an experiment. A prototype with two substrates was tested, but was found to have much greater rigidity than the single-sided substrate version. As this leaves electrical contacts exposed at one side, a layer of insulation was added as individual pieces to the adhesive on the copper tape which minimizes risk of short circuit across multiple elements and allows flexibility. The display is capable of a wide range of curvature sufficient to be used on forearms of all sizes.

Temperature control of the device at the skin interface was a main priority. Thin film resistive temperature detectors (RTDs) were placed at the end of each row for this measurement. The sensors used were TFD series flat element detectors from Omega, Inc. The sensor uses a platinum resistance detector created specifically for rapid, flat surface measurement. Rapid response is achieved by possessing a large surface-area to volume ratio along with a high-conductivity ceramic substrate [39]. The RTD works by experiencing linear changes in resistance as temperature fluctuates. When a voltage is applied to the sensor, the change in voltage potential across each RTD is monitored via

an input device and used to safely and effectively operate the thermal display. Figure 21 shows the overall control logic of the system. Phidgets, Inc, produces a variety of control boards commercially available that were used to perform the electrical tasks required. A 6-port USB hub is used to interface the sensor inputs to the control program. High current output was needed for the device (Up to 4.4 A) and is provided by a PWM motor controller which can continuously output up to 14 A. This device was also interfaced with the control program.

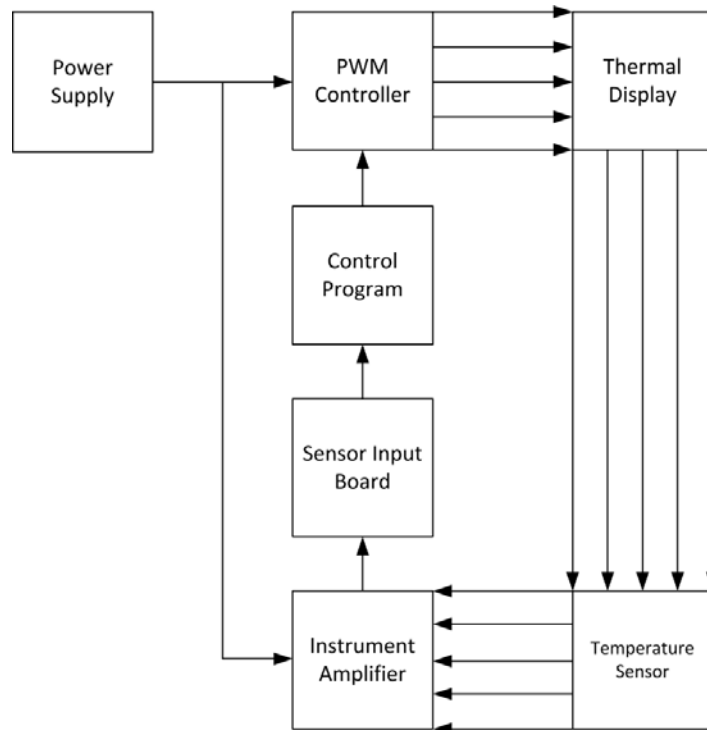


Figure 21 – Control flowchart for a thermal display with five independent thermoelectric rows.

To test the thermal grill effect with this device, the PWM controller will bring each row up to a maximum temperature in timed succession. Once the maximum temperature is reached in a particular row, it is slowly cooled at rate less perceivable than the heating. Figure 22 shows the principle graphically. As this process is repeated in a

loop, the thermal grill effect should cause the subjects to sense continual summation of temperature in close proximity, thus perceiving a sensation of constant heating under the pain threshold [18].

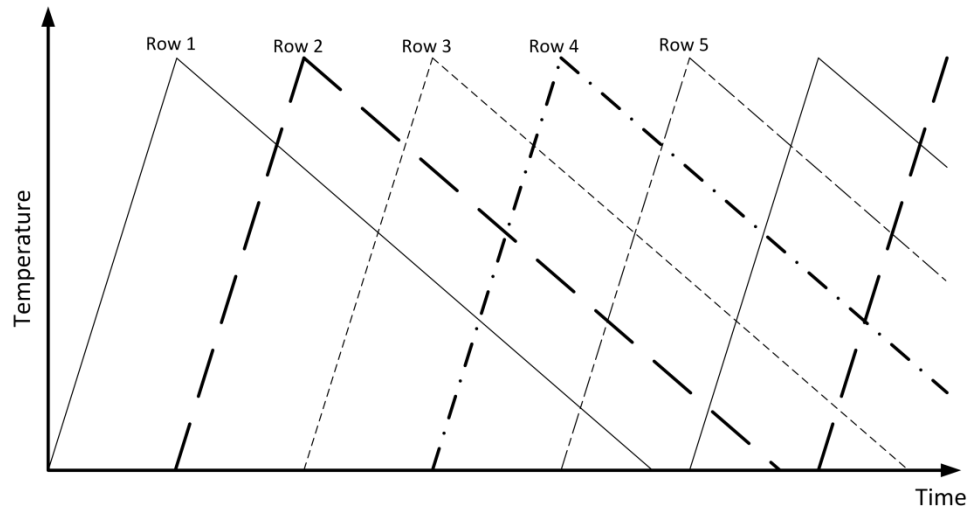


Figure 22 – Transient temperature control of five independent rows of thermoelectric elements. By applying the transient temperature to a subject, the thermal grill effect will be tested.

4.3 Simulated Performance

Static performance analysis of the device at different time steps was done, not only to visualize the control of the device, but also to determine if heat would be leaked into adjacent tissue areas where another row was interacting. One of the main deficiencies in current thermal display research is in the modeling of a system designed to predict the thermal performance at the receptor location. Yamamoto [40] developed a model, but only characterizes the cooler surface temperature based on thermal contact resistance between a finger tip and the device substrate. The model presented in this paper differs in the fact that is able to describe the temperature gradient at a particular

depth within the skin. Three tissue layers were modeled as epidermis, dermis and muscle tissue. Published values for thermal conductivity were found to be 0.209 W/mK, 0.322 W/mK, 0.419 W/mK for epidermis, dermis and muscle tissue respectively [41]. The Vinyl substrate located between the copper contact and epidermis layer was assigned conductivity as 0.311 W/mK based on a commercial used polymer tested in research [42]. The top side of the muscle layer was held constrained to mimic an internal body temperature (T_B) of 310 K and the substrate was held at room temperature at 298 K.

ELEMENT226 brick elements were again used to model the thermoelectric elements. ELEMENT227 tetrahedral elements were applied to the copper contact material again as well. The Seebeck Coefficient for this model was decreased to 170 $\mu\text{V/K}$ in this model to align better with typical bulk material properties [43]. The designated tissue volumes were meshed with SOLID87 tetrahedral elements. Because the tissue volumes contained a much larger number of nodes compared to the previous analyses, the mesh size had to be reduced to one-third the element width, or 1.2 mm. While this is not the most optimal size, it was seen in previous verifications that temperature gradients were not affected nearly as much as the heat flux results with mesh sizes of this order. This was verified by modeling only one row of the device which, with a mesh size equal to one-sixth the element height, was under the maximum node count. Figure 23 shows the agreement between temperatures in the direction of heat pumping between the coarse mesh size used in the analysis and a fine mesh.

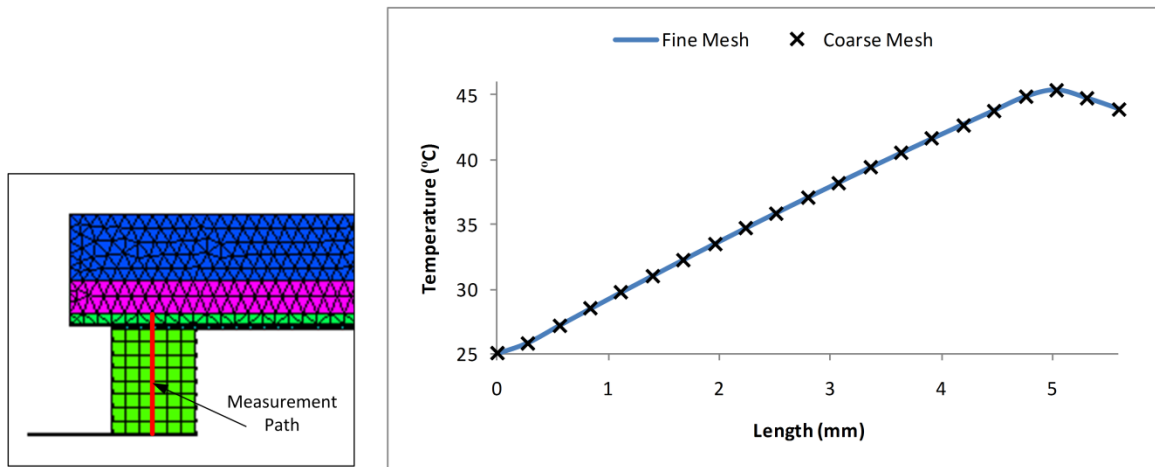


Figure 23 – Comparison of temperature profiles in the direction of heat flow for a coarse mesh and fine mesh size.

Since temperature is the important parameter in this analysis, the larger mesh size is used with confidence. Referring back to Figure 22, when any row is at its peak value, the rows in succession should be at 75%, 50%, 25% and 0% of the max value. By translating this to the model, current inputs for each time-step were divided based on this.

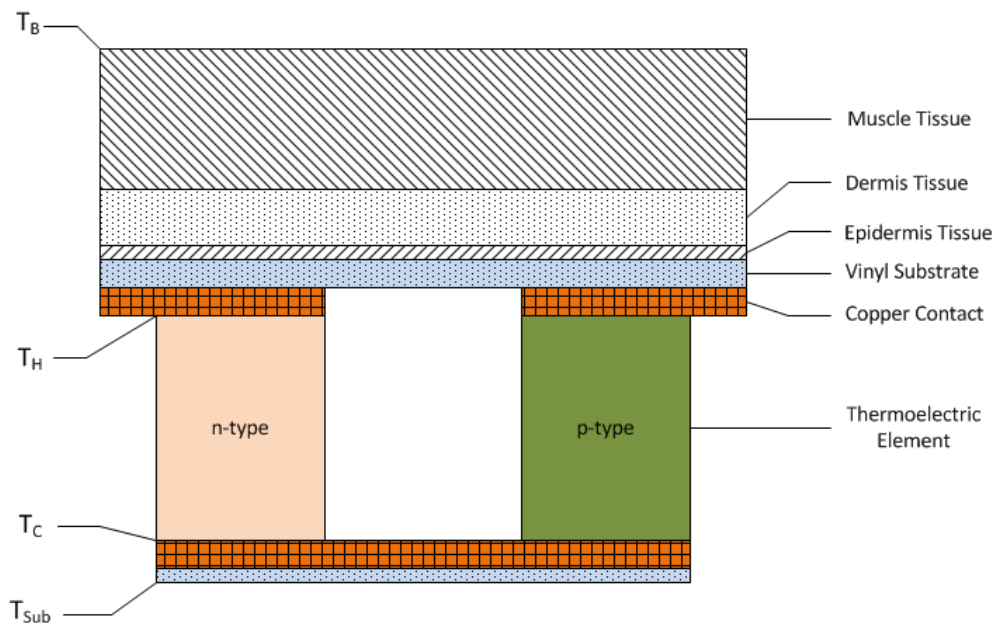


Figure 24 – Components and design of the FEA model simulating a haptic device on skin tissue.

Skin receptors are located at a shallow depth within the dermis layer of tissue. From the model, the epidermis-dermis interface temperature gradient will show how the thermal information is presented to the receptors. Figure 25 is a time step representation where the third row is at its maximum temperature. The maximum temperature shown for this condition at this interface is about 40 °C. The model shows hot-junction temperatures near what was crudely tested experimentally under the same current input along the third row. The physical experiment consisted of placing the prototype device seen in Figure 19 on a desk at 23 °C, applying a current via an adjustable current limiting power supply, and using a surface temperature probe to measure the topside surface while a finger was placed on top to act as a heat exit path at an element site. At a current of 3.0 A, a temperature of 42 °C was measured at the top surface. Considering exact material properties were not known for the macro-elements being used, this was considered satisfactory.

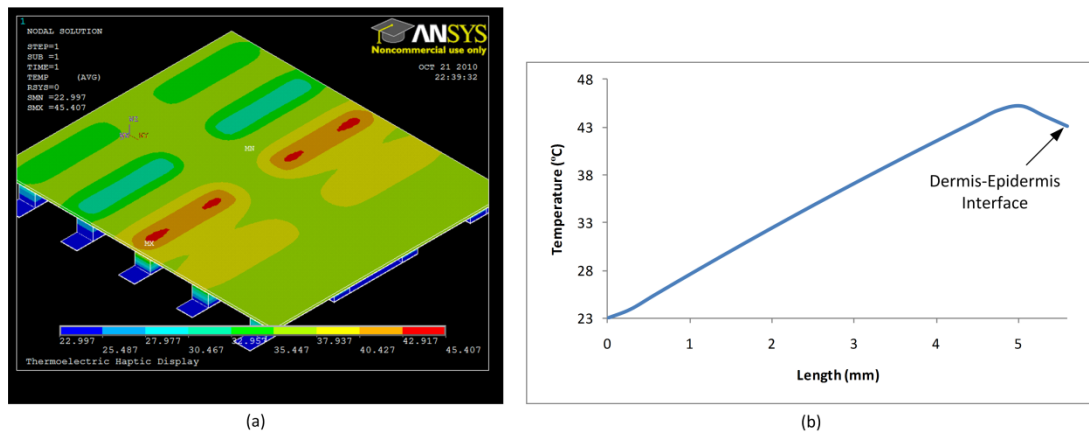


Figure 25 – (a) Temperature profile at the epidermis-dermis interface when the third thermoelectric row is at a maximum value, (b) Plot of the profile at the center of an element in Row 3.

At each time step in Figure 27, it is seen how the most active rows penetrate best into the dermis. This is desirable since the temperature receptor is most sensitive to changes in heat flux. As the time step transitions, this zone of higher energy is shown shifting from one row to the next, which describes the application of the thermal grill effect.

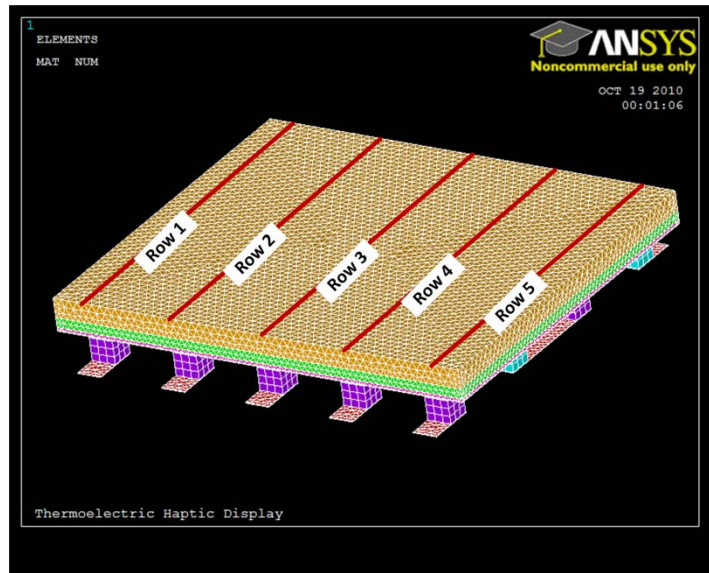


Figure 26 – Description of the orientation of discretely controlled thermoelectric rows.

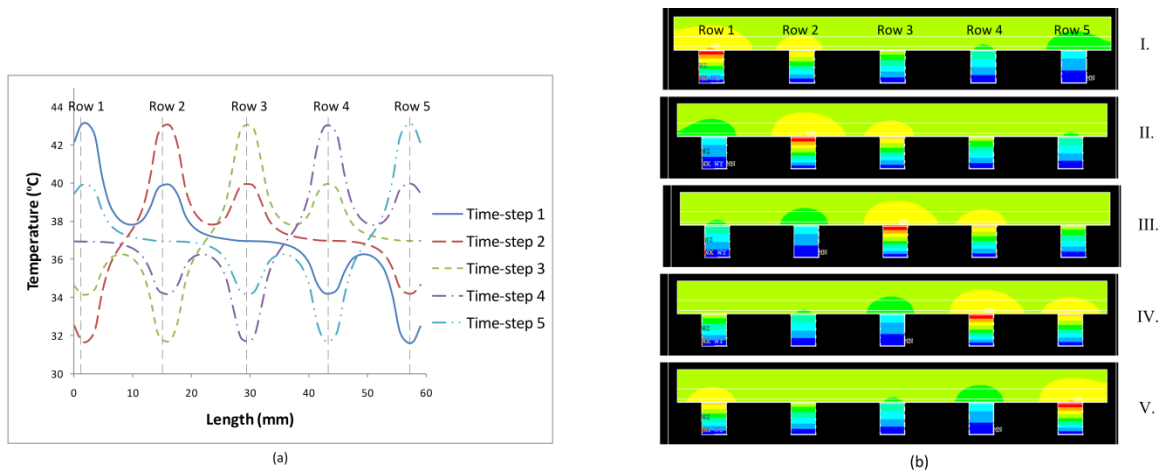


Figure 27 – (a) Plot of temperature profile along the interface between the epidermis and dermis. The path travels across each of the five thermoelectric rows, (b) Time step nodal contour map of the thermal display while testing the thermal grill effect.

4.4 Next Steps in Device Development

With the current simulation showing good performance characteristics under the given conditions, completion of the functional prototype will be the central focus. As progress is ongoing in the development of a functional prototype, various modifications are planned to improve the device. A constant temperature of the topside (non-skinside) will be maintained by use of a channeled pathway which will have a temperature controlled fluid flowing through it. Current development of this system is underway, where device flexibility retention is the main issue being worked. The second device improvement is in controlling the spatial dimensions of the individual elements. Because the first prototype devices have been built by hand, certain sacrifices to achieve initial testing were made. While soldering, elements tended to shift out of alignment. By creating a fixture to keep each element within the array from shifting linearly or radially,

a much better prototype can be built while still working in the convenience of our own lab.

Chapter 5 – Conclusions and Recommendations for Advancement

In this work, a review of the thermoelectric effect, its history and fundamental theory has been applied to analyzing modern systems of self-assembly and haptics. The effect, typically described using one-dimensional, thermodynamic conservation equations, was found to be insufficient in providing detailed information about local thermal effects caused by non-homogeneities introduced in a self-assembled system. A three-dimensional FEA model was created by writing an Ansys batch program which automated most of the steps required to perform an analysis for a 6x6 array of elements with a redundancy of 4.

In the modern one-dimensional models, non-ideal system characteristics are introduced by quantifying thermal contact resistance, entry and exit conduction regions and fill factor which have been shown to increase model accuracy at small size scales. Considering the sub-millimeter part sizes proposed for self-assembly processes, these non-traditional characteristics were deemed necessary to be included in the three-dimensional model. Methods for equating the two models were presented and verified through the comparison of simulation results. The first method varied current density over a range including the calculated optimal condition. Very good agreement was seen between junction temperature, and a basic correlation was seen between the cold junction heat flux values. As the mesh size was decreased during testing, better agreement was seen. Further refinement could not be made, unfortunately, due to a maximum node count

of 256,000 being reached with element size equal to one-sixth the length of a thermoelectric element. A further increase in agreement could be tested by submitting the batch code to CIRCE, a university computer more equipped to handle super-fine, high-node count models. The second model run at optimal conditions showed better agreement. An error of 0.47 W/cm² was seen between the two models, and was fairly consistent for each case. Further investigation could be done to find what drives this difference of consistent magnitude.

Analysis of the self-assembled case was done using a model similar to that of the verification. An ideal configuration was first simulated to provide a baseline for performance comparison. Unexpectedly, local performance within the center cluster tended to increase with a reduction of assembled elements as well as total heat flux at the cold junction. This occurred for the cases with two and three assembled elements. It was found, however, that the coefficient of performance decreased in the cases missing elements which describes a less efficient use of input power. For the case of only one assembled element, thermal performance degraded severely by displaying the domination of Joule heating within the single center element.

Finally, a project integrating haptics with thermoelectric devices was undertaken with the intention of designing, simulating, and building a thermal display with the capability to test the thermal grill effect. This was accomplished by assembling a device with five independently controlled rows, each containing four thermoelectric macro-scale elements. Temperature control was added by attaching thin dimension RTD's to the skin-side of an element. A commercially available signal input board will be used to receive temperature data and interface to a control program. Also, 5 channels of PWM DC motor

control will be interfaced to the control program and used to modulate the input current for each thermoelectric row of the display.

FEA was done to describe and model various discrete points in time within the inherently transient situation. As temperature receptors are, on average, 1 mm below the skin surface, the temperature gradient due to an applied surface temperature was analyzed to see how effective a thermal display can be at delivering the thermal information to a receptor. While static analysis showed good agreement and was powerful in describing how the temperature is presented to receptors within the dermis layer of tissue, improvement could be made here by performing a transient analysis of the various independent rows heating and cooling in the sequence described.

List of References

- [1] Seebeck, S. (1823). Magnetische Polarisation der Metalle und Erze durch Temperatur-Differenz. *Abhandlungen der Preussischen, Wissenschaften*, 265-373.
- [2] Goldsmid, H. Julian. (1964). *Thermoelectric Refrigeration*. Wembley, England: Plenum Press, NY.
- [3] Borelius, G., Keesom, W.H., Johansson, C.H., Linde, J.O. (1932). *Proc. Acad. Sci.-Amsterdam* 35, 10.
- [4] Altenkirch, E. (1911). *Phys. Z.* 12, 920.
- [5] Boncheva, M., Bruzewicz, D.A., Whitesides, G.M. (2003). Millimeter-scale self-assembly and its applications. *Pure Applied Chemistry* 75, 5, 621 – 630.
- [6] Wu, D.Y., Meure, S., Solomon, D. (2008). Self-healing polymeric materials: A review of recent developments. *Progress in Polymer Science* 33, 5, 479 – 522.
- [7] Bentley, R.E. (1998). The use of elemental thermocouples in high-temperature precision thermometry. *Measurement* 23, 35 – 46.
- [8] McGuire, M.A., Schmidt, A.M., Gascoin, F., Snyder, G.J., DiSalvo, F.J. (2006). Thermoelectric and structural properties of a new Chevrel phase: $Ti_{0.3}Mo_5RuSe_8$. *Journal of Solid State Chemistry* 179, 2158 – 2163.
- [9] MacDonald, D.K.C. (1962). *Thermoelectricity: and introduction to the principles*. Ottawa, Canada: John Wiley & Sons, Inc, NY.
- [10] Hou, P. Y., Baskaran, R., and Böhringer, K. F.,(2009)."Optimization of Microscale Thermoelectric Cooling (TEC) Element Dimensions for Hotspot Cooling Applications. *Journal of Electronic Materials*, 38 ,7, 950 - 953.
- [11] Fujimoto, S. (2007). Protections of the again of n-type Bi-Te thermoelectric cooling systems. *Journal of Alloys and Compounds* 443, 182-190.
- [12] Harman, T.C., Honig, J.M. (1967). *Thermoelectric and Thermomagnetic Effects and Applications*. New York, New York: McGraw-Hill Book Company.
- [13] Ho, H. (2007). Development and Evaluation of a Thermal Model for Haptic interfaces. Ph.D. Dissertation. *Massachusetts Institute of Technology*.

- [14] Pelesko, J.A. (2007). Self Assembly: The Science of Things That Put Themselves Together. Boca Raton, FL: *Chapman & Hall/CRC*, 4-176.
- [15] Nomoto, S. et al. (2004). Role of body afferent pathways of heat and cold in body temperature regulation. *International Journal of Biometeorology* 49, 67-85.
- [16] Jones, L.A. (2008). Warm or Cool, Large or Small? The challenge of Thermal Displays. *IEEE Transactions of Haptics* 1, 53-70.
- [17] Deml, B., et al. (2006). Development and Experimental Evaluation of a Thermal Display. *Proc. EuroHaptics Conf*, 257-262.
- [18] Yang, G. (2009). Spatial Acuity and Summation on the Hand: The Role of Thermal Cues in Material Discrimination. *Attention, Perception, & Psychophysics* 71, 156-163.
- [19] Yamamoto, A. et al. (2004). Control of Thermal Tactile Display Based on Predictions of Contact Temperature. *Proceedings from IEEE International Conference of Robotics and Automation*, 1536-1541.
- [20] Green, B.G. (2004). Temperature Perception and Nociception. *Journal of Neurobiology* 61, 13 – 29.
- [21] MacLean, K.E., Roderick, J.B. (1999). Smart Tangible Displays in the Everyday World: A haptic Door Knob. *Proceeding from the Int'l Conference on Advanced Intelligent Mechatronics*, 203 – 208.
- [22] Bolanowski, S. J. et al. (1988). Four Channels Mediate the Mechanical Aspects of Touch. *Journal of Accustical Soc. of Am.* 84, 1680-1694.
- [23] Bolanowski, S. J. et al. (1982). Temperature and Criterion Effects in a Somatosensory Subsystem: A Neurophysiological and Psychophysical Study. *Journal of Neurophysiology* 48, 836-855.
- [24] Johnson, K.O. et al. (1973). Peripheral Neural Determinants of Temperature Discrimination in Man: A Correlative Study of Responses to Cooling Skin. *Journal of Neurophysiology* 36, 347-370.
- [25] Duclaux, R. et al. (1972). The Temperature Sensitivity of the Type I Slowly Adapting Mechanoreceptors in Cats and Monkeys. *Journal of Physiology* 224, 647-664.
- [26] Darian-Smith, I. et al. (1977). Thermal Sensibility and Thermal Receptors. *Journal of Investigative Dermatology* 69, 146-153.
- [27] Ansys, Inc. (2009). Ansys Academic Research release v12.1 product documentation. *Help System, Thermal-Electric Analysis, Chapter 2.2.*
- [28] Antonova, E. E. (2005). Finite Elements for Thermoelectric Device Analysis in Ansys. *International Conference on Thermoelectrics*, 200-203.

- [29] Gin, G. (1999). Cooling performance of integrated thermoelectric microcooler. *Solid-State Electronics* 43, 5, 923-929.
- [30] Yim, W.M., Fitzke, E., Rosi, F.D. (1966). Thermoelectric Properties of $\text{Bi}_2\text{Te}_3\text{-Sb}_2\text{Se}_3$ Pseudo-Ternary Alloys in the Temperature Range 77 to 300 K. *Journal of Material Science* 1, 52-65.
- [31] Bottner, H., Nurnus, J., Gavrikov, A., Kuhner, G., Jagle, M., Kunzel, C., Eberhard, D. Plescher, G., Shubert, A., Schlerch, K. (2004). New Thermoelectric Components Using Microsystem Technologies. *Journal of Microelectromechanical Systems* 13, 1, 414 – 420.
- [32] Venkatasubramanian, R. (2004). Superlattice Thermoelectric Technology. DOE/EPRI high Efficiency Thermoelectrics Workshop. San Diego, CA.
- [33] Marlow. (2006). Marlow Industries, product specifications. <http://www.marlow.com>.
- [34] Crane, N., Mishra, P., Murray Jr., J.L., Nolas, G.L. (2009) Self-Assembly for Integration of Microscale Thermoelectric Coolers. *Journal of Electronic Materials*, 38, 7, 1252 – 1256.
- [35] Miner, A. (2007). The Compatibility of Thin Films and Nanostructures in Thermoelectric Cooling Systems. *Journal of Heat Transfer* 129, 805-812.
- [36] Ziolkowski, P. (2010). Estimation of Thermoelectric Generator Performance by Finite Element Modeling. *Journal of Electronic Materials*.
- [37] Defrin, R., Benstein-Sheraizin, A., Bezalel, A., Mantzur, O., Arendt-Nielsen, L. (2008). The spatial characterization of the painful thermal grill illusion. *Pain* 138, 577 – 586.
- [38] Green, B.G. (2002). Synthetic heat at mild temperatures. *Somatosens Mot Res*, 19, 130 – 138.
- [39] Omega, Inc. (2010). Thin Film Detector – Flat RTD Element Product Specification Documentation. http://www.omega.com/ppt/pptsc.asp?ref=TFD_RT&bt=cart.
- [40] Yamamoto, A., Hashimoto, H., Higuchi, T. (2003). Tactile Display for presenting thermal characteristics of materials based on prediction of contact temperature. Proceedings from the 8th Annual Conference of the Virtual Reality Society of Japan, 233-236.
- [41] Cohen, M.L. (1977). Measurement of the Thermal Properties of Human Skin. A Review. *The Journal of Investigative Dermatology*, 69, 333 – 338.
- [42] Ghose, S., Watson, K.A., Working, D.C., Connell, J.W., Smith, J.G., Sun, Y.P. (2008). Thermal conductivity of ethylene vinyl acetate copolymer/nanofiller blends. *Composites Science and Technology* 68, 1843 – 1853.
- [43] Kou, C.H., Hwang, C.S., Jeng, M.S., Su, W.S., Chou, Y.W., Ku, J.R. (2010). Thermoelectric transport properties of bismuth telluride bulk materials fabricated by ball milling and spark plasma sintering. *Journal of Alloys and Compounds* 496, 687 – 690.

Appendices

Appendix A – Ansys Batch Code

A.1 Micro-thermoelectric Cooler

```
/title, Thermoelectric Cooler 6X6 R=4
/VUP, 1, z
/VIEW, 1, 1, 1, 1
/TRIAD, OFF
/NUMBER, 1
/PNUM, MAT, 1
/nopr

/PREP7
! Element size/number
N =36
S =sqrt(N)
le =2e-4
h =2e-4
ch =2.5e-5
sub =5.0e-5
sink =7.5e-5

!Array Characteristics
R =4
f =0.9

!Electric Conditions
J =1.3485e7 !Current density (A/m^2)
I =J*R*le*le !Current to be applied

!Source and Sink Temps
Ts = 300
Ta = 325

spc =(S*le/sqrt(f) - S*le) / (S - 1)

!toffst, 273

! Material Properties
K = 2
! n-type
mp, rsvx, 1, 1.0e-5 !Resistivity
mp, kxx, 1, K !Th. Conductivity
mp, sbkx, 1, -240e-6 !Seebeck

! p-type
mp, rsvx, 2, 1.0e-5 !Resistivity
mp, kxx, 2, K !Th. Conductivity
mp, sbkx, 2, 240e-6 !Seebeck

! Contacts
mp, rsvx, 3, 1.7e-8 !Resistivity
mp, kxx, 3, 400 !Th. Conductivity

! Substrate
mp, rsvx, 4, 1e6
Kch = 1e6 !Conductance (W/m^2K)
g = 0.0001
K_star = K/g !Thermal contact conductance (W/m^2K)
Kche = (Kch*K_star*f)/(Kch+K_star*f)
```


Appendix A (continued)

khce = Kche*(sub+sink)
mp, kxx, 4, khce !Th. Conductivity

! Element types

et, 1, 226, 110

et, 2, 227, 110

et, 3, solid87

!Block model element

block, - (5*spc/2+2*le), - (5*spc/2+3*le), , le, , h ! 1N

block, - (3*spc/2+le), - (3*spc/2+2*le), , le, , h ! 2N

block, - (5*spc/2+2*le), - (5*spc/2+3*le), spc+le, spc+2*le, , h ! 3N

block, - (3*spc/2+le), - (3*spc/2+2*le), spc+le, spc+2*le, , h ! 4N

block, 3*spc/2+le, 3*spc/2+2*le, , le, , h ! 5N

block, 5*spc/2+2*le, 5*spc/2+3*le, , le, , h ! 6N

block, 3*spc/2+le, 3*spc/2+2*le, spc+le, spc+2*le, , h ! 7N

block, 5*spc/2+2*le, 5*spc/2+3*le, spc+le, spc+2*le, , h ! 8N

block, - (spc/2), - (spc/2+le), 2*spc+2*le, 2*spc+3*le, , h ! 9N

block, spc/2, spc/2+le, 2*spc+2*le, 2*spc+3*le, , h ! 10N

block, - (spc/2), - (spc/2+le), 3*spc+3*le, 3*spc+4*le, , h ! 11N

block, spc/2, spc/2+le, 3*spc+3*le, 3*spc+4*le, , h ! 12N

block, - (5*spc/2+2*le), - (5*spc/2+3*le), 4*spc+4*le, 4*spc+5*le, , h ! 13N

block, - (3*spc/2+le), - (3*spc/2+2*le), 4*spc+4*le, 4*spc+5*le, , h ! 14N

block, - (5*spc/2+2*le), - (5*spc/2+3*le), 5*spc+5*le, 5*spc+6*le, , h ! 15N

block, - (3*spc/2+le), - (3*spc/2+2*le), 5*spc+5*le, 5*spc+6*le, , h ! 16N

block, 3*spc/2+le, 3*spc/2+2*le, 4*spc+4*le, 4*spc+5*le, , h ! 17N

block, 5*spc/2+2*le, 5*spc/2+3*le, 4*spc+4*le, 4*spc+5*le, , h ! 18N

block, 3*spc/2+le, 3*spc/2+2*le, 5*spc+5*le, 5*spc+6*le, , h ! 19N

block, 5*spc/2+2*le, 5*spc/2+3*le, 5*spc+5*le, 5*spc+6*le, , h ! 20N

block, - (spc/2), - (spc/2+le), , le, , h ! 21P

block, spc/2, spc/2+le, , le, , h ! 22P

block, - (spc/2), - (spc/2+le), spc+le, spc+2*le, , h ! 23P

block, spc/2, spc/2+le, spc+le, spc+2*le, , h ! 24P

block, - (5*spc/2+2*le), - (5*spc/2+3*le), 2*spc+2*le, 2*spc+3*le, , h ! 25P

block, - (3*spc/2+le), - (3*spc/2+2*le), 2*spc+2*le, 2*spc+3*le, , h ! 26P

block, - (5*spc/2+2*le), - (5*spc/2+3*le), 3*spc+3*le, 3*spc+4*le, , h ! 27P

block, - (3*spc/2+le), - (3*spc/2+2*le), 3*spc+3*le, 3*spc+4*le, , h ! 28P

block, 3*spc/2+le, 3*spc/2+2*le, 2*spc+2*le, 2*spc+3*le, , h ! 29P

block, 5*spc/2+2*le, 5*spc/2+3*le, 2*spc+2*le, 2*spc+3*le, , h ! 30P

block, 3*spc/2+le, 3*spc/2+2*le, 3*spc+3*le, 3*spc+4*le, , h ! 31P

block, 5*spc/2+2*le, 5*spc/2+3*le, 3*spc+3*le, 3*spc+4*le, , h ! 32P

block, - (spc/2), - (spc/2+le), 4*spc+4*le, 4*spc+5*le, , h ! 33P

block, spc/2, spc/2+le, 4*spc+4*le, 4*spc+5*le, , h ! 34P

block, - (spc/2), - (spc/2+le), 5*spc+5*le, 5*spc+6*le, , h ! 35P

block, spc/2, spc/2+le, 5*spc+5*le, 5*spc+6*le, , h ! 36P

!Block model contacts

block, - (5*spc/2+4*le), - (3*spc/2+le), , spc+2*le, h, h+ch

block, - (5*spc/2+3*le), (spc/2+le), , spc+2*le, , -ch

block, - (spc/2+le), 5*spc/2+3*le, , spc+2*le, h, h+ch

Appendix A (continued)

```
bl ock, 3*spc/2+1e, 5*spc/2+3*1e, , 3*spc+4*1e, , - ch
bl ock, - (spc/2+1e), 5*spc/2+3*1e, 2*spc+2*1e, 3*spc+4*1e, h, h+ch
bl ock, spc/2+1e, - (5*spc/2+3*1e), 2*spc+2*1e, 3*spc+4*1e, , - ch
bl ock, - (5*spc/2+3*1e), - (3*spc/2+1e), 2*spc+2*1e, 5*spc+6*1e, h, h+ch
bl ock, - (5*spc/2+3*1e), spc/2+1e, 4*spc+4*1e, 5*spc+6*1e, , - ch
bl ock, - (spc/2+1e), 5*spc/2+3*1e, 4*spc+4*1e, 5*spc+6*1e, h, h+ch
bl ock, 3*spc/2+1e, 5*spc/2+4*1e, 4*spc+4*1e, 5*spc+6*1e, , - ch
```

!Block model substrate

```
bl ock, - (5*spc/2+3*1e), (5*spc/2+3*1e), , 5*spc+6*1e, h+ch, h+ch+sub
bl ock, - (5*spc/2+3*1e), (5*spc/2+3*1e), , 5*spc+6*1e, - ch, - (ch+sub)
```

!Block model sink and source mass

```
bl ock, - (5*spc/2+3*1e), (5*spc/2+3*1e), , 5*spc+6*1e, - (ch+sub), -
(ch+sub+si nk)
bl ock, - (5*spc/2+3*1e), (5*spc/2+3*1e), , 5*spc+6*1e, h+ch+sub,
h+ch+sub+si nk
vgl ue, al l
```

!Mesh Control

!TE elements

esi ze, 1e/6

type, 1

mat, 1

vmesh, 1

vmesh, 2

vmesh, 3

vmesh, 4

vmesh, 5

vmesh, 6

vmesh, 7

vmesh, 8

!vmesh, 9

vmesh, 10

vmesh, 11

vmesh, 12

vmesh, 13

vmesh, 14

vmesh, 15

vmesh, 16

vmesh, 17

vmesh, 18

vmesh, 19

vmesh, 20

mat, 2

vmesh, 21

vmesh, 22

vmesh, 23

vmesh, 24

vmesh, 25

vmesh, 26

vmesh, 27

vmesh, 28

vmesh, 29

vmesh, 30

vmesh, 31

Appendix A (continued)

v mesh, 32
v mesh, 33
v mesh, 34
v mesh, 35
v mesh, 36

! Contacts
! size, l e/4
type, 2
mat, 3
v mesh, 53, 54
v mesh, 57, 64

! Substrate
! size, l e/3
type, 3
mat, 4
v mesh, 55, 56

! Sink/Source Mass
v mesh, 51, 52

! Boundary Conditions
! Sink Mass
n sel, s, l oc, z, - (ch+sub+si nk)
d, all, temp, Ts

! Source Mass
n sel, s, l oc, z, h+ch+sub+si nk
d, all, temp, Ta

n sel, s, l oc, z, - ch
nr=ndnext(0)

! Apply Electric
! Terminal ground
! A276 is lead surface
n sel, s, l oc, x, (5*spc/2+4*le)
d, all, volt, 0

! Terminal apply current
! A221 is lead surface
n sel, s, l oc, x, - (5*spc/2+4*le)
cp, 1, volt, all
ni=ndnext(0)
f, ni, amps, I

n sel, all
fi ni

! SOLUTIONS
/SOLU
antype, static
solve
fi ni

! POST PROCESSING
/POST1
pl nsol, temp

Appendix A (continued)

```
!Top surface temperature profile
PATH, path1, 2, 30, 50
PPATH, 1, 0, (1e+spc)/2, 0, 1e, 0,
PPATH, 2, 0, (1e+spc)/2, (6*1e+5*spc), 1e, 0,
Appendix A (Continued)
```

```
PDEF, , TEMP, , AVG
PLPATH, TEMP
```

```
!Bottom surface temperature profile
PATH, path2, 2, 30, 50
PPATH, 1, 0, (1e+spc)/2, 0, 0, 0,
PPATH, 2, 0, (1e+spc)/2, (6*1e+5*spc), 0, 0,
PDEF, , TEMP, , AVG
PLPATH, TEMP
```

```
!Full side temperature profile at edge
PATH, path3, 2, 30, 20
PPATH, 1, 0, (1e+spc)/2, 1e/2, -(ch+sub+sink), 0,
PPATH, 2, 0, (1e+spc)/2, 1e/2, (h+ch+sub+sink), 0,
PDEF, , TEMP, , AVG
PLPATH, TEMP
```

```
!Center element temperature profile
PATH, path4, 2, 30, 20
PPATH, 1, 0, -(1e+spc)/2, 7*1e/2, 0, 0,
PPATH, 2, 0, -(1e+spc)/2, 7*1e/2, 1e, 0,
PDEF, , TEMP, , AVG
PLPATH, TEMP
```

```
!Edge element temperature profile
PATH, path5, 2, 30, 20
PPATH, 1, 0, (1e+spc)/2, 1e/2, 0, 0,
PPATH, 2, 0, (1e+spc)/2, 1e/2, 1e, 0,
PDEF, , TEMP, , AVG
PLPATH, TEMP
```

```
!=====List Heat Rates at Ts Boundary=====!
nselect, s, loc, z, -(ch+sub+sink)
nplot
prsol, HEAT

fini
```

A.2 Haptic Display

```
/title, Thermolectric Haptic Display
/VUP, 1, z
/VIEW, 1, 1, 1, 1
/TRIAD, OFF
/NUMBER, 1
/PNUM, MAT, 1
/nopr

/PREP7
! Element size/number

rs =0.0100
```

Appendix A (Continued)

es =0. 0125
le =0. 0038
h =0. 0048
ch =1. 0e-4
sub =1. 0e-4
epi d=5. 0e-4
derm=1. 5e-3
musc=3. 0e-3

toffst, 273

Ts =23
Tb =37

Ii =-0
Iii =-0
Iiii=-3
Iiv =-0
Iv =-0

! Material Properties

K = 2

! n-type

mp, rsvx, 1, 1. 0e-5 !Resistivity
mp, kxx, 1, K !Th. Conductivity
mp, sbkx, 1, -170e-6 !Seebeck

! p-type

mp, rsvx, 2, 1. 0e-5 !Resistivity
mp, kxx, 2, K !Th. Conductivity
mp, sbkx, 2, 170e-6 !Seebeck

! Contacts

mp, rsvx, 3, 1. 7e-8 !Resistivity
mp, kxx, 3, 400 !Th. Conductivity

! Substrate

mp, kxx, 4, 0. 25

!Epi dermis

mp, kxx, 5, 0. 209

!Dermis

mp, kxx, 6, 0. 322

!muscle

mp, kxx, 7, 0. 419

! Element types

et, 1, 226, 110
et, 2, 227, 110
et, 3, solid87

!Block model elements

!Row 1 n-type

block, -(2*le+3*es/2), -(le+3*es/2), , le, , h
block, es/2, le+es/2, , le, , h

!Row 2 n-type

Appendix A (continued)

block, $-(2^*1e+3^*es/2)$, $-(1e+3^*es/2)$, $1e+rs$, 2^*1e+rs , , h
block, $es/2$, $1e+es/2$, $1e+rs$, 2^*1e+rs , , h

!Row 3 n-type

block, $-(2^*1e+3^*es/2)$, $-(1e+3^*es/2)$, 2^*1e+2^*rs , 3^*1e+2^*rs , , h
block, $es/2$, $1e+es/2$, 2^*1e+2^*rs , 3^*1e+2^*rs , , h

!Row 4 n-type

block, $-(2^*1e+3^*es/2)$, $-(1e+3^*es/2)$, 3^*1e+3^*rs , 4^*1e+3^*rs , , h
block, $es/2$, $1e+es/2$, 3^*1e+3^*rs , 4^*1e+3^*rs , , h

!Row 5 n-type

block, $-(2^*1e+3^*es/2)$, $-(1e+3^*es/2)$, 4^*1e+4^*rs , 5^*1e+4^*rs , , h
block, $es/2$, $1e+es/2$, 4^*1e+4^*rs , 5^*1e+4^*rs , , h

!Row 1 p-type

block, $-(1e+es/2)$, $-(es/2)$, , $1e$, , h
block, $1e+3^*es/2$, $2^*1e+3^*es/2$, , $1e$, , h

!Row 2 p-type

block, $-(1e+es/2)$, $-(es/2)$, $1e+rs$, 2^*1e+rs , , h
block, $1e+3^*es/2$, $2^*1e+3^*es/2$, $1e+rs$, 2^*1e+rs , , h

!Row 3 p-type

block, $-(1e+es/2)$, $-(es/2)$, 2^*1e+2^*rs , 3^*1e+2^*rs , , h
block, $1e+3^*es/2$, $2^*1e+3^*es/2$, 2^*1e+2^*rs , 3^*1e+2^*rs , , h

!Row 4 p-type

block, $-(1e+es/2)$, $-(es/2)$, 3^*1e+3^*rs , 4^*1e+3^*rs , , h
block, $1e+3^*es/2$, $2^*1e+3^*es/2$, 3^*1e+3^*rs , 4^*1e+3^*rs , , h

!Row 5 p-type

block, $-(1e+es/2)$, $-(es/2)$, 4^*1e+4^*rs , 5^*1e+4^*rs , , h
block, $1e+3^*es/2$, $2^*1e+3^*es/2$, 4^*1e+4^*rs , 5^*1e+4^*rs , , h

!Block Contacts

block, $-(3^*1e+3^*es/2)$, $-(1e+3^*es/2)$, , $1e$, , $-ch$
block, $-(3^*1e+3^*es/2)$, $-(1e+3^*es/2)$, $1e+rs$, 2^*1e+rs , , $-ch$
block, $-(3^*1e+3^*es/2)$, $-(1e+3^*es/2)$, 2^*1e+2^*rs , 3^*1e+2^*rs , , $-ch$
block, $-(3^*1e+3^*es/2)$, $-(1e+3^*es/2)$, 3^*1e+3^*rs , 4^*1e+3^*rs , , $-ch$
block, $-(3^*1e+3^*es/2)$, $-(1e+3^*es/2)$, 4^*1e+4^*rs , 5^*1e+4^*rs , , $-ch$

block, $-(2^*1e+3^*es/2)$, $-(es/2)$, , $1e$, h , $h+ch$
block, $-(2^*1e+3^*es/2)$, $-(es/2)$, $1e+rs$, 2^*1e+rs , h , $h+ch$
block, $-(2^*1e+3^*es/2)$, $-(es/2)$, 2^*1e+2^*rs , 3^*1e+2^*rs , h , $(h+ch)$

Appendix A (continued)

block, $-(2^*1e+3^*es/2)$, $-(es/2)$, 3^*1e+3^*rs , 4^*1e+3^*rs , h , $h+ch$
block, $-(2^*1e+3^*es/2)$, $-(es/2)$, 4^*1e+4^*rs , 5^*1e+4^*rs , h , $h+ch$

block, $-(1e+es/2)$, $(1e+es/2)$, , $1e$, , $-ch$
block, $-(1e+es/2)$, $(1e+es/2)$, $1e+rs$, 2^*1e+rs , , $-ch$
block, $-(1e+es/2)$, $(1e+es/2)$, 2^*1e+2^*rs , 3^*1e+2^*rs , , $-ch$
block, $-(1e+es/2)$, $(1e+es/2)$, 3^*1e+3^*rs , 4^*1e+3^*rs , , $-ch$
block, $-(1e+es/2)$, $(1e+es/2)$, 4^*1e+4^*rs , 5^*1e+4^*rs , , $-ch$

block, $es/2$, $2^*1e+3^*es/2$, , $1e$, h , $h+ch$
block, $es/2$, $2^*1e+3^*es/2$, $1e+rs$, 2^*1e+rs , h , $h+ch$
block, $es/2$, $2^*1e+3^*es/2$, 2^*1e+2^*rs , 3^*1e+2^*rs , h , $h+ch$

Appendix A (continued)

block, es/2, 2*1e+3*es/2, 3*1e+3*rs, 4*1e+3*rs, h, h+ch
block, es/2, 2*1e+3*es/2, 4*1e+4*rs, 5*1e+4*rs, h, h+ch

block, 1e+3*es/2, 3*1e+3*es/2, , 1e, , - ch
block, 1e+3*es/2, 3*1e+3*es/2, 1e+rs, 2*1e+rs, , - ch
block, 1e+3*es/2, 3*1e+3*es/2, 2*1e+2*rs, 3*1e+2*rs, , - ch
block, 1e+3*es/2, 3*1e+3*es/2, 3*1e+3*rs, 4*1e+3*rs, , - ch
block, 1e+3*es/2, 3*1e+3*es/2, 4*1e+4*rs, 5*1e+4*rs, , - ch

!Substrate

block, - (5*1e/2+3*es/2), (5*1e/2+3*es/2), - 1e, 6*1e+4*rs, h+ch, h+ch+sub

block, - (3*1e+3*es/2), - (1e+3*es/2), , 1e, - ch, - (ch+sub)
block, - (3*1e+3*es/2), - (1e+3*es/2), 1e+rs, 2*1e+rs, - ch, - (ch+sub)
block, - (3*1e+3*es/2), - (1e+3*es/2), 2*1e+2*rs, 3*1e+2*rs, - ch, - (ch+sub)
block, - (3*1e+3*es/2), - (1e+3*es/2), 3*1e+3*rs, 4*1e+3*rs, - ch, - (ch+sub)
block, - (3*1e+3*es/2), - (1e+3*es/2), 4*1e+4*rs, 5*1e+4*rs, - ch, - (ch+sub)

block, - (1e+es/2), (1e+es/2), , 1e, - ch, - (ch+sub)
block, - (1e+es/2), (1e+es/2), 1e+rs, 2*1e+rs, - ch, - (ch+sub)
block, - (1e+es/2), (1e+es/2), 2*1e+2*rs, 3*1e+2*rs, - ch, - (ch+sub)
block, - (1e+es/2), (1e+es/2), 3*1e+3*rs, 4*1e+3*rs, - ch, - (ch+sub)
block, - (1e+es/2), (1e+es/2), 4*1e+4*rs, 5*1e+4*rs, - ch, - (ch+sub)

block, 1e+3*es/2, 3*1e+3*es/2, , 1e, - ch, - (ch+sub)
block, 1e+3*es/2, 3*1e+3*es/2, 1e+rs, 2*1e+rs, - ch, - (ch+sub)
block, 1e+3*es/2, 3*1e+3*es/2, 2*1e+2*rs, 3*1e+2*rs, - ch, - (ch+sub)
block, 1e+3*es/2, 3*1e+3*es/2, 3*1e+3*rs, 4*1e+3*rs, - ch, - (ch+sub)
block, 1e+3*es/2, 3*1e+3*es/2, 4*1e+4*rs, 5*1e+4*rs, - ch, - (ch+sub)

!Tissue

block, - (5*1e/2+3*es/2), (5*1e/2+3*es/2), -
1e, 6*1e+4*rs, h+ch+sub, h+ch+sub+epi d
block, - (5*1e/2+3*es/2), (5*1e/2+3*es/2), -
1e, 6*1e+4*rs, h+ch+sub+epi d, h+ch+sub+epi d+derm
block, - (5*1e/2+3*es/2), (5*1e/2+3*es/2), -
1e, 6*1e+4*rs, h+ch+sub+epi d+derm, h+ch+sub+epi d+derm+musc
vgl ue, all

!Mesh Control

!Elements

size, 1e/3
type, 1
mat, 1
vmesh, 1, 10
mat, 2
vmesh, 11, 20

!Contacts

size, 1e/4
type, 2
mat, 3
vmesh, 83, 92
vmesh, 94, 106, 3
vmesh, 93, 105, 3
vmesh, 95, 107, 3

!Substrate

type, 3
mat, 4

Appendix A (continued)

vmesh, 108

!Epi dermi s
mat, 5
vmesh, 80

!Dermi s
mat, 6
vmesh, 81

!Muscl e
esi ze, 1e/3
mat, 7
vmesh, 82

!====Boundary Condi ti ons=====
!Source Temp
nse l, s, l oc, z, - ch
d, all, temp, Ts

!Body Temp
nse l, s, l oc, z, h+ch+sub+epi d+derm+musc
d, all, temp, Tb

!====Termi nal Ground=====
!Row 1
!nse l, s, l oc, x, - (3*1e+3*es/2)
!nse l, r, l oc, y, , 1e
nse l, s, l oc, x, (3*1e+3*es/2)
nse l, r, l oc, y, , 1e
d, all, vol t, 0

!Row 2
!nse l, s, l oc, x, - (3*1e+3*es/2)
!nse l, r, l oc, y, 1e+rs, 2*1e+rs
nse l, s, l oc, x, (3*1e+3*es/2)
nse l, r, l oc, y, 1e+rs, 2*1e+rs
d, all, vol t, 0

!Row 3
!nse l, s, l oc, x, - (3*1e+3*es/2)
!nse l, r, l oc, y, 2*1e+2*rs, 3*1e+2*rs
nse l, s, l oc, x, (3*1e+3*es/2)
nse l, r, l oc, y, 2*1e+2*rs, 3*1e+2*rs
d, all, vol t, 0

!Row 4
!nse l, s, l oc, x, - (3*1e+3*es/2)
!nse l, r, l oc, y, 3*1e+3*rs, 4*1e+3*rs
nse l, s, l oc, x, (3*1e+3*es/2)
nse l, r, l oc, y, 3*1e+3*rs, 4*1e+3*rs
d, all, vol t, 0

!Row 5
!nse l, s, l oc, x, - (3*1e+3*es/2)
!nse l, r, l oc, y, 4*1e+4*rs, 5*1e+4*rs
nse l, s, l oc, x, (3*1e+3*es/2)
nse l, r, l oc, y, 4*1e+4*rs, 5*1e+4*rs
d, all, vol t, 0

Appendix A (continued)

```
!====Terminal Current Input====!  
!Row 1  
nset, s, loc, x, -(3*1e+3*es/2)  
nset, r, loc, y, , 1e  
!nset, s, loc, x, (3*1e+3*es/2)  
!nset, r, loc, y, , 1e  
ni=ndnext(0)  
cp, 1, volt, all  
f, ni, amps, Ii  
  
!Row 2  
nset, s, loc, x, -(3*1e+3*es/2)  
nset, r, loc, y, 1e+rs, 2*1e+rs  
!nset, s, loc, x, (3*1e+3*es/2)  
!nset, r, loc, y, 1e+rs, 2*1e+rs  
nii=ndnext(0)  
cp, 2, volt, all  
f, nii, amps, Iii  
  
!Row 3  
nset, s, loc, x, -(3*1e+3*es/2)  
nset, r, loc, y, 2*1e+2*rs, 3*1e+2*rs  
!nset, s, loc, x, (3*1e+3*es/2)  
!nset, r, loc, y, 2*1e+2*rs, 3*1e+2*rs  
niii=ndnext(0)  
cp, 3, volt, all  
f, niii, amps, Iiii  
  
!Row 4  
nset, s, loc, x, -(3*1e+3*es/2)  
nset, r, loc, y, 3*1e+3*rs, 4*1e+3*rs  
!nset, s, loc, x, (3*1e+3*es/2)  
!nset, r, loc, y, 3*1e+3*rs, 4*1e+3*rs  
niv=ndnext(0)  
cp, 4, volt, all  
f, niv, amps, Iiv  
  
!Row 5  
nset, s, loc, x, -(3*1e+3*es/2)  
nset, r, loc, y, 4*1e+4*rs, 5*1e+4*rs  
!nset, s, loc, x, (3*1e+3*es/2)  
!nset, r, loc, y, 4*1e+4*rs, 5*1e+4*rs  
nv=ndnext(0)  
cp, 5, volt, all  
f, nv, amps, Iv  
  
nset, all  
fini  
!Solution  
/SOLU  
antype, static  
solve  
fini  
  
!Post Processing  
/POST1  
plnsol, temp
```

Appendix A (continued)

!Full side temperature profile at edge

PATH, path1, 2, 30, 20

PPATH, 1, 0, $3 \cdot l e / 2 + 3 \cdot e s / 2$, $(5 \cdot l e / 2 + 2 \cdot r s)$, - (ch), 0,

PPATH, 2, 0, $3 \cdot l e / 2 + 3 \cdot e s / 2$, $(5 \cdot l e / 2 + 2 \cdot r s)$, (h+ch+sub+epi d), 0,

PDEF, , TEMP, , AVG

PLPATH, TEMP

!Top surface profile

PATH, path2, 2, 30, 50

PPATH, 1, 0, $(l e + e s) / 2$, 0, h+ch+sub+epi d, 0,

PPATH, 2, 0, $(l e + e s) / 2$, $5 \cdot l e + 4 \cdot r s$, h+ch+sub+epi d, 0,

PDEF, , TEMP, , AVG

PLPATH, TEMP

fi ni

Appendix B – Matlab Analytical Solutions Code

B.1 Plotting T_C , T_H , and Q versus Current Density

```
%System Properties
Ta = 325;          %T ambient (K)
Ts = 300;          %T heat sink (K)
Kh = 10^6;         %Exit conductance (W/m^2K)
Kc = 10^6;         %Entrance conductance (W/m^2K)
k = 2.0;           %Element conductivity (W/mK)
S = 240e-6;       %Seeback coef (V/K)
I = [0: .1: 4];   %Input current (A)
r = 1e-5;         %Element resistivity (Ohm-m)
f = 0.9;          %Fill factor
n = 0.01;         %Redundancy
R = 4;            %Redundancy

%Element dimensions
Le = 2e-4;        %Element thickness (m)

%RE
RE = 1e-8;        %Electrical contact resistance (ohm-m^2)
RE = r*Le*(1+2*n);

%K, Khe and Kce
g = 1e-4;         %Ratio of TE conductivity and contact conductivity
(Thermal) (m)
Kstar = k/g;      %Thermal contact conductance (W/m^2K)
Khe = Kh*Kstar*f/(Kh+Kstar*f); %Exit thermal conductance (W/m^2K)
Kce = Kc*Kstar*f/(Kc+Kstar*f); %Entry thermal conductance (W/m^2K)
K = k/Le;        %Equivalent element conductance (W/m^2K)

for i=1: 1: length(I)
    %Current
    %Current Density (A/m^2)
    J(i) = I(i)/R/Le^2;
    %Simultaneous energy equations
    A = [J(i)*S+K+Kce/f - K ; K J(i)*S- K- Khe/f];
    C = [Kce/f*Ts+0.5.*J(i). *J(i)*RE ; -Khe/f*Ta-0.5*J(i). *J(i). *RE];
    X = A\C;

    Tc(i) = X(1); %Cold J-n temperature (K)
    Th(i) = X(2); %Hot J-n temperature (K)
    Qp(i) = J(i). *S*Tc(i) - J(i). *J(i). *RE/2 - K*(Th(i)-Tc(i)); %Heat
flux (W/m^2)
    Qp2(i) = f*Qp(i)/10000; %Heat flux (Total area units) (W/cm^2K)
    Qcrane(i) = Kce*(Ts- Tc(i))/10000;
    P(i) = RE*J(i)^2+J(i)*S*(Th(i)-Tc(i));
end
```

Appendix B (continued)

$$J = J'$$

$$T_c = T_c'$$

$$T_h = T_h'$$

$$Q_{p2} = Q_{p2}'$$

$$Q_{crane} = Q_{crane}'$$

$$P'$$

$$\%Q_{crane} = K_{ce} * (T_s - T_c) / 10000$$